Vehicle-bridge interaction and driving accident risks under skew winds

A. Camara

Department of Civil Engineering. City, University of London. Northampton Square, London, EC1V 0HB, United Kingdom

Abstract

This paper proposes a new methodology to simulate wind fields that are non-orthogonal to the structure and to the traffic direction, and it presents the first wind-vehicle-bridge interaction (W-VBI) analysis framework to account for skew wind effects on the driving safety. The three-directional skew wind fields that are generated match well the target frequency content and correlation properties along the deck. The W-VBI methodology is applied to the study of vehicles crossing a long bridge for a wide range of wind incidence angles. It is observed that even though purely cross-winds increase the vehicle-bridge interaction, skew headwinds are more likely to cause driving accidents.

Keywords:
Skew winds; stochastic wind simulation; driving accidents; vehicle-bridge interaction; time-history analysis

1. Introduction

Wind-driven traffic interruptions and accidents represent a major problem in a large number of bridges around the world [1]. The risk of vehicle accidents is higher in long-span bridges because they are usually exposed to strong winds and have slender decks prone to vibrations. The assessment of the driving accident risks of vehicles crossing bridges in windy environments involves a complex wind-vehicle-bridge interaction (W-VBI) problem. This is generally solved with semi-analytical models that define the direct wind

Email address: alfredo.camara@city.ac.uk (A. Camara)

actions on the bridge and on the vehicles from their aerodynamic coefficients, and solve the equations of motion for the deck, the vehicle and their interaction under wind loading at every time-step. This approach is repeated in numerous works (see e.g. [2, 3, 4, 5]) but, to the author's knowledge, in all of them the mean wind speed is assumed to be perpendicular to the deck of the bridge. However, skew winds are usually more dangerous from the point of view of the vehicle stability and also more likely to occur [6, 7, 8]. This work proposes a new W-VBI method that accounts for non-orthogonal wind directions.

In the driving safety analysis the effect of the skewness of the wind is materialized both in the dynamic response of the bridge and of the vehicles crossing it. This paragraph is dedicated to the structural response of bridges without vehicles subject to skew winds, for which A. Davenport and his co-authors were pioneers [9, 10]. In the traditional buffeting analysis skew winds are treated with the so-called 'cosine rule' by which the along-flow wind speed is decomposed into two perpendicular components: one normal to the deck, and the other parallel to it (driving direction) that is ignored. The normal and the vertical wind components are used in conjunction with the aerodynamic coefficients of the true (orthogonal) deck cross-section obtained from sectional model tests (experimental or numerical). Scanlan [6] proposed a refinement of this approach by modifying the flutter derivatives in terms of the wind incidence (yaw or skew) angle between the mean wind speed and the deck (β), and analysing the response in the frequency domain. However, Zhu *et al.* [7, 8] observed in the wind tunnel testing of the Tsing Ma Bridge that the previous approaches can be significantly inaccurate for very skew winds. These authors observed that the drag coefficient of the deck decreases and its pitching moment coefficient increases by increasing the wind incidence angle β, with the lift being almost instensitive to it. More recently, it has been observed experimentally in the Third Nanjing Bridge that the most unfavorable buffeting responses of the bridge are not associated with purely cross-winds ($\beta = 90°$) but with yaw angles between $\beta = 60°$ and $85°$ [11]. Xie *et al.* [12] introduced an effective mean wind speed and a turbulent correlation length to account for skew winds in the conventional frequency-domain definition of the wind turbulence field. However, this methodology is only valid for yaw angles close to $\beta = 90°$ (i.e. cross-winds) and the cross-correlation between wind components was ignored. In addition, the buffeting analysis was done entirely in the frequency domain, for which the W-VBI problem is not readily established.

In terms of the response of vehicles in off-bridge conditions, Batista *et al.* [13] proposed a detailed driving stability analysis based on the wheel reactions obtained from static equilibrium in different types of vehicles under purely cross-winds ($\beta = 90°$). This wind direction was assumed to be critical in [13], however, Baker [14] demonstrated with a dynamic model of a 4-wheeled vehicle that the wind incidence angles that are between $\beta = 30°$ and $60°$ are more dangerous for the driving stability of vans and tractors with trailers driving off-bridge. More recently, Kim *et al.* [15] proposed a probabilistic approach to assess the driving-induced accident risks in vehicles crossing bridges. They adopted the static model presented in [13] but accounted for the disturbance in the wind flow introduced by the shape of the deck on different road lanes, and the results also identified that the range of wind incidence angles between $\beta = 30°$ and $60°$ were critical. However, the assessment of the vehicle accient risks in [15] was based on a static analysis that ignores the effect of the wind gusts, the pavement irregularities and the vehicle/bridge dynamic responses, as well as their interaction. The latter is considered in several works focusing on the W-VBI problem (e.g. [2, 3, 4, 5]) but they are particuarised for the specific case of purely cross-winds.

This paper represents the first attempt to include the effect of the wind incidence angle in a detailed W-VBI analysis. To this end, a proposal to simulate skew wind fields is formulated as an extension of the widely accepted methodology of Veers [16]. It is observed that the resulting non-orthogonal wind fields match well the target frequency content and correlation properties along the deck. These are introduced in a genernal W-VBI framework that accounts for the wind incidence angle as well as the coherence of pavement irregularity profiles in the transverse direction (across-deck). The methodology is applied to the study of a long-span bridge with variable cross-section under skew winds interacting with traffic actions modelled with multi-degree-of-freedom (MDOF) vehicles. The results demonstrate that purely cross-winds increase the dynamic response of the deck and the vehicle-bridge interaction at the central span, but skew headwinds with incidence angles between $\beta = 40°$ and $70°$ maximise the risk of driving accidents in high-sided vehicles.

2. Mean off-bridge vehicle actions

First, the influence of the apparent wind incidence angle (β) on the mean aerodynamic actions on a high-sided vehicle is examined. The steady wind effects on a vehicle are given as

$$f_{v,w}^{l} = \frac{1}{2}\rho U_r^2 C_l^v(\psi) A_v, \text{ with } l = D, S, L \tag{1a}$$

$$f_{v,w}^{l} = \frac{1}{2}\rho U_r^2 C_l^v(\psi) A_v h_v, \text{ with } l = Y, P, R, \tag{1b}$$

where $l = D, S, L$ refers to the drag, side and lift forces, respectively, and $l = Y, P, R$ to the yaw, pitch and roll moments; ρ is the density of the air, taken as 1.225 kg/m^3 in this work; U_r is the relative wind speed acting on the vehicle; $C_l^v(\psi)$ are the static coefficents, which depend on the relative wind incidence angle ψ; A_v is the front area of the vehicle; h_v is the vertical distance between the centroid of the vehicle and its wheel-pavement contact. The aerodynamic coefficients of the vehicle can be calculated from expressions that are adjusted to the results of wind tunnel testing reported in [13, 14], which considered the vehicles situated in homogeneous wind fields free from obstacles (i.e. off-bridge conditions). In the case of a large van or a rigid truck, when $0° \leq \psi \leq 90°$:

$$C_S^v = \sigma_1 \psi^{0.382} \tag{2a}$$

$$C_L^v = \sigma_2[1 + \sin(3\psi)] \tag{2b}$$

$$C_D^v = \sigma_3[1 + 2\sin(3\psi)] \tag{2c}$$

$$C_Y^v = -\sigma_4 \psi^{1.77} \tag{2d}$$

$$C_P^v = \sigma_5 \psi^{1.32} \tag{2e}$$

$$C_R^v = \sigma_6 \psi^{0.924}, \tag{2f}$$

with ψ in radians. When $90° < \psi \leq 180°$ the same expressions included above can be used after changing the incidence angle by $\psi = 180° - \psi$ and converting it to radians. The values of the parameters σ_1 to σ_6 can be found in [13, 14] for different types of vehicles, based on which Fig. 1 presents the side and rolling aerodynamic coefficients for all possible wind incidence angles. These two actions have a strong influence in the overall vehicle accident risk, and they are maximised when the effective wind incidence angle is perpendicular to the vehicle, regardless of its typology. The same effect can be observed in the yaw and the pitch coefficients.

The relative wind speed (U_r) and the relative wind incidence angle (ψ) depend on the aparent wind velocity vector and on the vehicle speed (V_d),

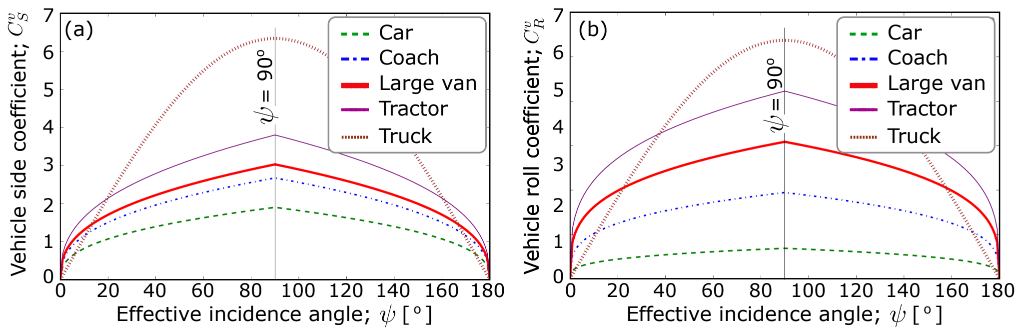

Figure 1: Aerodynamic coefficients in terms of the effective wind incidence angle ψ given in [13, 14] for different types of vehicles; (a) side coefficient C_S^v, (b) roll coefficient C_R^v.

as it is shown in Fig. 2 for two different driving directions. In this study the apparent wind incidence angle β is defined as the angle between the vehicle path (in x-direction) and the wind direction.

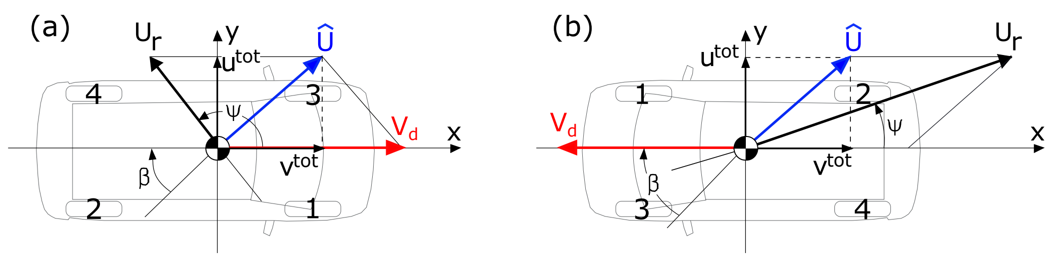

Figure 2: Relative wind/driving velocity ignoring turbulence and considering two scenarios with $\beta < 90°$: (a) driving in the positive-x direction, (b) driving in the negative-x direction. The numbers 1-4 represent the wheel ordering. The convention for positive wind incidence angles in this study is also included.

The vector diagrams included in Fig. 2 can be expressed mathematically as:

$$U_r^2 = (v^{tot} - V_d)^2 + (u^{tot})^2 \tag{3}$$

$$\psi = \arctan\left(\frac{u^{tot}}{v^{tot} - V_d}\right), \tag{4}$$

where u^{tot} and v^{tot} are the across-drive (parallel to the axis y) and the along-drive (parallel to x) projections of the total wind speed; if turbulence is ignored $u^{tot} = \widehat{U}\sin(\beta)$ and $v^{tot} = \widehat{U}\cos(\beta)$, with $\widehat{U}$ representing the mean along-flow wind speed. Also note that $V_d > 0$ in Eqs. (3) and (4) if the vehicle moves in the positive-x direction (Fig. 2(a)), and $V_d < 0$ otherwise (Fig. 2(b)).

Fig. 3 shows the wind actions on a high-sided vehicle moving in the negative-x direction with a speed of $V_d = -30$ m/s. The results are given in terms of the apparent wind incidence angle β and the along-flow mean wind speed normalised with respect to the driving speed ($\widehat{U}/V_d$), ignoring the effect of turbulence. Fig. 3(a) includes the normalised effective wind-vehicle velocity U_r, which is significantly affected by the skew angle of the wind. Tailwinds occur if $\beta > 90°$ because $V_d < 0$ and this leads to reduced values of U_r, reaching a zero value for the limit case in which $\beta = 180°$ and the mean wind speed coincides with the vehicle speed. However, headwinds ($\beta < 90°$) increase the relative wind speed on the vehicle, reaching its peak when $\beta = 0°$ and the vehicle speed adds directly to the wind speed. Fig. 3(b) presents the effective wind incidence angle ψ and it shows that skew tailwinds with certain speeds can create the effect of cross-winds ($\psi = 90°$) on the vehicle, for which the aerodynamic coefficients C_S^v and C_R^v are maximised according to Fig. 1. It is also observed that wind incidence angles β below 90° that increase U_r have associated low values of ψ even for very large wind speeds, and this reduces the aerodynamic forces on the vehicles.

Fig. 3(b) includes the wind-induced side force in the van studied in [14], calculated from Eq. (1a). It is observed that headwinds are critical from the point of view of the vehicle stability, particularly with β ranging from 40° to 60°. This is explained by the fact that U_r is larger when $\beta < 90°$ and it is squared in the calculation of the aerodynamic forces in Eq. (1), although decrements of β below 20° result in a rapid reduction of the wind side force because the value of ψ and the corresponding aerodynamic coefficient are small. It is important to note that purely cross-winds are not critical for the side wind force on the vehicle, specially for large wind speeds. These results will be confirmed in the detailed W-VBI analysis including turbulent wind, pavement irregularities and vehicle-bridge dynamic interaction effects that were ignored in this section.

3. Generation of skew wind fields

The W-VBI assessment of the driving accident risks requires the simulation of the wind velocity field at discrete points of the bridge. If the deck is

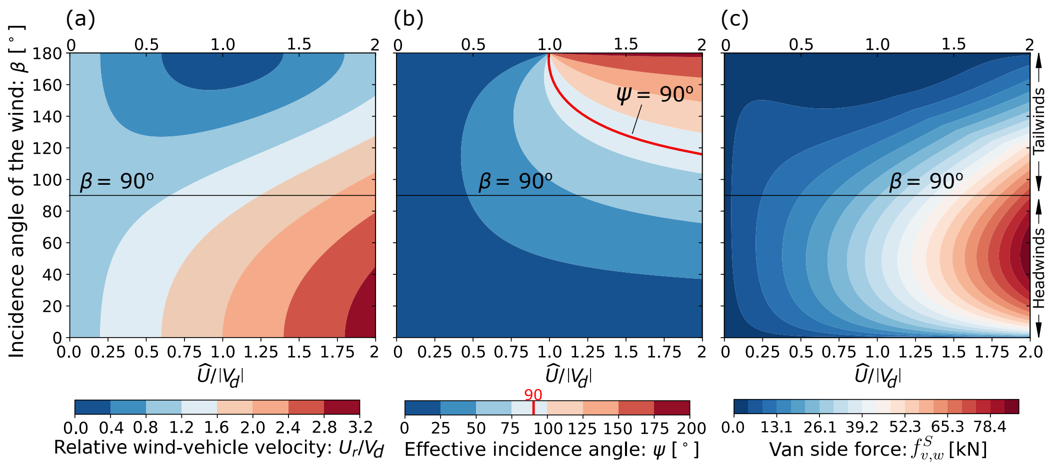

Figure 3: Mean effect of the wind incidence angle (β) on: (a) the relative wind speed in the vehicle (U_r), (b) the effective incidence angle of the wind in the vehicle (ψ), and (c) the side force in a van ($f^S_{v,w}$). Results obtained for a vehicle driving speed of $V_d = -30$ m/s (i.e. in the negative-x direction) and ignoring turbulence.

straight in plan, the N_p points along its length in which wind is simulated are contained in a vertical plane that is referred to as the *Structural Plane*, or SP in short. The existing methods to generate wind velocity signals assume that the SP is perpendicular to the direction of the mean wind flow, i.e. they are only valid for cross-winds. Previous works on W-VBI implicitly assume the same scenario. However, considering only cross-winds can underestimate the wind actions on the vehicles, as it was demonstrated in the simplified analysis conducted in Section 2. This Section proposes an extension of the methodology introduced by Veers [16] to generate realistic three-directional (3D) spatially distributed pseudo-random wind time-histories that are non-orthogonal to the SP.

The idea is to define an auxiliary plane where Veer's methodology can be directly applied because it is perpendicular to the along-flow mean wind velocity. This plane is referred to as *Generation Plane* (GP) because it is where the wind velocity histories are generated. The GP is vertical, located upwind from the structure and forming an angle β with the normal of the SP, as shown in Fig. 4. The wind field in the GP is defined by superimposing the along-flow mean wind speed ($\widehat{U}$) to zero-mean turbulence components generated at the orthogonal projections of the N_p structural nodes. Note that in this work the symbol $\widehat{\cdot}$ is used to represent properties in the reference system of the GP: $\widehat{x}, \widehat{y}, \widehat{z}$, with $\widehat{x}$ being the across-flow horizontal direction, $\widehat{y}$ the along-flow horizontal direction, and $\widehat{z}$ the vertical direction, which is always parallel to the z axis in the SP. The turbulence time-histories associated with the j-th node of the structure projected in the GP in the directions $\widehat{x}$, $\widehat{y}$ and $\widehat{z}$ are referred to as $\widehat{v}_j(t)$, $\widehat{u}_j(t)$ and $\widehat{w}_j(t)$, respectively. These turbulence components start at the GP ($t = 0$ s), but due to the distance between the GP and the SP they arrive at the node j in the SP at time t^*, with a delay Δt_j with respect to the projected node in the GP. Δt_j can be calculated by accepting the Taylor's hypothesis of frozen turbulence in which $\widehat{u}_j(t)$, $\widehat{v}_j(t)$ and $\widehat{w}_j(t)$ travel in the along-flow direction with the mean wind speed corresponding to that node: $\widehat{U}_j(z_j)$ (where z_j is the height of the j-th node above the ground).

Fig. 4(a) shows that in the particular case of purely cross-winds ($\beta = 90°$) this time-lag is the same in all the nodes at the same height. In fact, if $\beta = 90°$ the axes of the GP are parallel to those in the SP and both can be coincident, implying that $t = t^*$ and the turbulence components in the structural axes (x, y, z), referred to as u_j, v_j and w_j for the across-deck, along-deck and vertical components, respectively, are directly $\widehat{u}_j(t) \equiv u_j(t^*)$, $\widehat{v}_j(t) \equiv v_j(t^*)$ and $\widehat{w}_j(t) \equiv w_j(t^*)$. However, if $\beta \neq 90°$ the GP is not parallel to the SP and therefore the wind velocity signals arrive to the structure asynchronously with a varying time-lag that is highlighted in red colour in the three wind velocity time-histories included for illustration purposes in Fig. 4(b), and therefore $\widehat{u}_j(t) \neq u_j(t^*)$, $\widehat{v}_j(t) \neq v_j(t^*)$ and $\widehat{w}_j(t) \neq w_j(t^*)$.

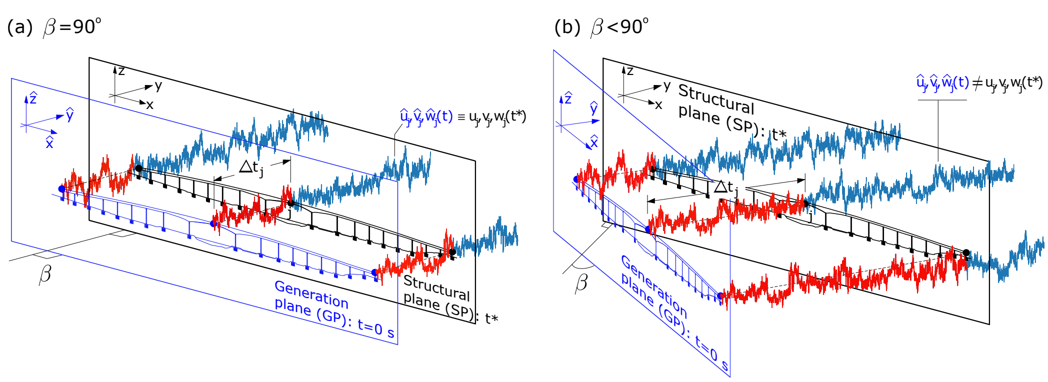

Figure 4: Time lags Δt_j (in red colour) between the start of the wind velocity signals ($t = 0$ s) and the instant in which they reach the structure under: (a) purely cross-winds ($\beta = 90°$), and (b) skew winds ($\beta \neq 90°$).

The generation of non-orthogonal wind fields proposed in this work is divided in four steps discussed in the following paragraphs along with the assumptions made.

Step 1: Project the structure in the GP

It is assumed that the N_p nodes of the structure are contained in a vertical plane that includes the structural axis z and thus only their along-drive horizontal coordinate (x) needs to be projected in the GP. This is shown in the plan view of the GP and the SP included in Fig. 5. A distance d_{jk} between two generic nodes j and k in the SP with coordinates (x_j, z_j) and (x_k, z_k), respectively, becomes in the GP:

$$\widehat{d}_{jk} = \sqrt{(x_j - x_k)^2 \sin^2(\beta) + (z_j - z_k)^2}. \tag{5}$$

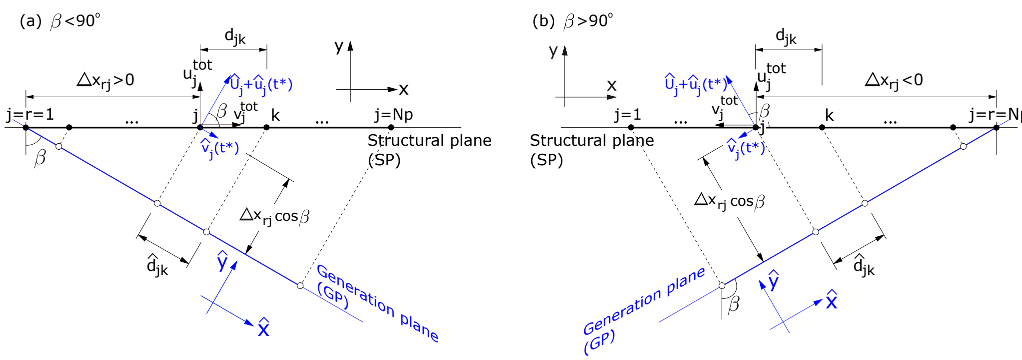

Figure 5: Plan view of the GP and the SP for two wind incidence angles: (a) $\beta < 90°$, (b) $\beta > 90°$.

Step 2: Generate wind signals perpendicular to the GP

The method of Shinozuka and Jan [17] is used to generate N_p correlated 3D velocity signals in the GP from the projected spectral matrix $\widehat{\mathbf{S}}^i$ associated with the i-th component of the turbulence in the GP axes, with $i = \widehat{u}, \widehat{v}, \widehat{w}$:

$$\widehat{\mathbf{S}}^i(f_m) = \begin{bmatrix} \widehat{S}^i_{11} & \dots & \widehat{S}^i_{1j} & \dots & \widehat{S}^i_{1N_p} \\ \vdots & \ddots & \vdots & \ddots & \vdots \\ \widehat{S}^i_{j1} & \dots & \widehat{S}^i_{jj} & \dots & \widehat{S}^i_{jN_p} \\ \vdots & \ddots & \vdots & \ddots & \vdots \\ \widehat{S}^i_{N_p1} & \dots & \widehat{S}^i_{N_pj} & \dots & \widehat{S}^i_{N_pN_p} \end{bmatrix}, \tag{6}$$

where f_m is the central frequency of the m-th frequency band in which the spectral densities are discretised. Considering that they are divided in N_f frequency bands of equal width Δf, the diagonal terms of $\widehat{\mathbf{S}}$ are defined as $\widehat{S}^i_{jj}(f_m) = \widehat{G}^i_{jj}(f_m)\Delta f$, in which $\widehat{G}^i_{jj}$ is the symmetric power spectral density (PSD) of the wind speed at node j in the direction i of the GP, and the off-diagonal term $\widehat{S}^i_{jk}(f_m)$ represents the cross-spectral density between the GP nodes j and k:

$$\widehat{S}^i_{jk}(f_m) = \widehat{\gamma}^i_{jk}(f_m)\Delta f \sqrt{\widehat{G}^i_{jj}(f_m)\widehat{G}^i_{kk}(f_m)}, \tag{7}$$

in which the spatial coherence between the wind velocity signals of two generic nodes in the GP ($\widehat{\gamma}^i_{jk}$) is defined from the coherence function based on their SP coordinates (x, z) projected in the GP

$$\widehat{\gamma}^i_{jk}(f_m) = \exp\left(\frac{-f_m\sqrt{[C^i_{\widehat{x}}(x_j - x_k)\sin(\beta)]^2 + [C^i_{\widehat{z}}(z_j - z_k)]^2}}{\widehat{U}_{jk}}\right), \tag{8}$$

where $\widehat{U}_{jk}$ is the arithmetic mean of the along-flow mean wind speeds at nodes j and k: $\widehat{U}_{jk} = (\widehat{U}_j + \widehat{U}_k)/2$; $C^i_{\widehat{x}}$ and $C^i_{\widehat{z}}$ are the coherence decrements in the horizontal (across-flow) and the vertical directions of the GP, respectively. It is noted that the difference between the coherence function defined in the SP (γ^i_{jk}) and the projected one considered in this work ($\widehat{\gamma}^i_{jk}$) is in the term affected by $\sin(\beta)$, with $\gamma^i_{jk} = \widehat{\gamma}^i_{jk}$ if $\beta = 90°$ and $\gamma^i_{jk} < \widehat{\gamma}^i_{jk}$ otherwise. This indicates that in the GP the wind velocity signals are more correlated than in the SP for skew winds.

The complex coefficient matrix $\widehat{\mathbf{V}}^i(f_m)$ in the i-th direction of the GP (with $i = \widehat{u}, \widehat{v}, \widehat{w}$) is obtained from the Cholesky decomposition of the spectral matrices $\widehat{\mathbf{S}}^i$ following [16, 17]. The inverse Fourier transform of each element of $\widehat{\mathbf{V}}^i(f_m)$ gives the turbulence wind velocity time series at the GP

$$\widehat{u}_j(t) = \sum_{m=1}^{N_f} \sqrt{2}\widehat{A}^{\widehat{u}}_{jm} \cos(2\pi f_m t - \widehat{\phi}^{\widehat{u}}_{jm}) \tag{9a}$$

$$\widehat{v}_j(t) = \sum_{m=1}^{N_f} \sqrt{2}\widehat{A}^{\widehat{v}}_{jm} \cos(2\pi f_m t - \widehat{\phi}^{\widehat{v}}_{jm}) \tag{9b}$$

$$\widehat{w}_j(t) = \sum_{m=1}^{N_f} \sqrt{2}\widehat{A}^{\widehat{w}}_{jm} \cos(2\pi f_m t - \widehat{\phi}^{\widehat{w}}_{jm}), \tag{9c}$$

where $\widehat{A}^i_{jm}$ and $\widehat{\phi}^i_{jm}$ are the components of the matrices $\widehat{\mathbf{A}}^i = \mathrm{mod}(\widehat{\mathbf{V}}^i)$ and $\widehat{\boldsymbol{\phi}}^i = \arg(\widehat{\mathbf{V}}^i)$, with the operators mod() and arg() representing the modulus and the argument of each of the complex variables included in $\widehat{\mathbf{V}}^i$, respectively.

Step 3: Shift the reference time to t^*

It is shown in Fig. 5 that the turbulence wind histories that start at $t = 0$ s in the GP reach their corresponding nodes in the SP at different instants. The time-delay that spans from the start of the signal at the j-th point of the GP to the moment in which it reaches the corresponding node in the SP is referred to as Δt_j. It can be obtained from the Taylor's hypothesis by assuming that the turbulence travels with the along-flow mean wind speed at that point ($\widehat{U}_j$) as:

$$\Delta t_j = \frac{\Delta x_{jr} \cos(\beta)}{\widehat{U}_j}, \tag{10}$$

$\Delta x_{jr} = x_j - x_r$ being the relative distance in the x direction of the SP defined between the node j and a reference point r contained at the intersection between the SP and the GP (for which $\Delta t_r = 0$ s). If $\beta < 90°$ the reference point is selected for convenience as the first node of the structure in the x direction (i.e. $r = 1$) to minimise Δt_j, as shown in Fig. 5(a). However, if $\beta > 90°$ the reference point is considered as the last node in the x direction (i.e. $r = N_p$) as illustrated in Fig. 5(b), which results in positive time-lags for any point in Eq. (10) since $\Delta x_{jN_p} < 0$ and $\cos(\beta) < 0$ when $\beta > 90°$. In the special case with $\beta = 90°$ the GP is defined as coincident with the SP so that $\Delta t_j = 0$ s and there is no need to define a reference point

After calculating Δt_j for all the points of the structure, their 3D turbulence components are referred to the nodes of the SP by removing from the original signals the corresponding time-lags

$$\widehat{u}_j(t^*) = \widehat{u}_j(t - \Delta t_j) \tag{11a}$$

$$\widehat{v}_j(t^*) = \widehat{v}_j(t - \Delta t_j) \tag{11b}$$

$$\widehat{w}_j(t^*) = \widehat{w}_j(t - \Delta t_j), \tag{11c}$$

with $t \geq \Delta t_j$ for any j.

Step 4: Rotate the wind signals to the axes of the SP

Finally, the wind signals parallel to the GP axes $(\widehat{x}, \widehat{y}, \widehat{z} \equiv z)$ are rotated to align them to the reference axes of the structure in the SP (x, y, z), as it is depicted in Fig. 5. Because the along-flow mean wind speed is generally not perpendicular to the SP, it is necessary to rotate the *total* wind velocity signals (mean speed plus turbulence) as

$$u^{tot}(t^*) = [\widehat{U}_j + \widehat{u}(t^*)]\sin(\beta) - \widehat{v}(t^*)\cos(\beta) \tag{12a}$$

$$v^{tot}(t^*) = [\widehat{U}_j + \widehat{u}(t^*)]\cos(\beta) + \widehat{v}(t^*)\sin(\beta) \tag{12b}$$

$$w^{tot}(t^*) = \widehat{w}(t^*), \tag{12c}$$

and not only their turbulence components. It is remarked that the time-histories resulting from Eq. (12) are the *total* wind velocity components, and that the along-flow mean wind speed $\widehat{U}_j$ affects both the perpendicular and the longitudinal wind components in the SP (u^{tot} and v^{tot}, respectively). However, the turbulent components in the SP may be needed by the aerodynamic model of choice, as it is discussed in the next section. These can be obtained by subtracting from the total horizontal wind components the mean wind speed projected to the corresponding SP axis:

$$u(t^*) = u^{tot}(t^*) - \bar{U}_{y,j} \tag{13a}$$

$$v(t^*) = v^{tot}(t^*) - \bar{U}_{x,j} \tag{13b}$$

$$w(t^*) = w^{tot}(t^*), \tag{13c}$$

with $\bar{U}_{y,j}$ and $\bar{U}_{x,j}$ being the across- and along-deck projections of the along-flow mean wind speed, respectively:

$$\bar{U}_{y,j} = \widehat{U}_j \sin(\beta) \tag{14a}$$

$$\bar{U}_{x,j} = \widehat{U}_j \cos(\beta). \tag{14b}$$

The above methodology is valid for wind incidence angles β in the range $[0°, 180°]$, and the cases with $\beta > 180°$ can be obtained by symmetry. In the particular scenario with $\beta = 90°$, i.e. for purely cross-winds, $\widehat{\gamma}^i_{jk} = \gamma^i_{jk}$ and $\widehat{S}^i_{jk} = S^i_{jk}$, resulting in $\widehat{u}(t^*) = u(t^*), \widehat{v}(t^*) = v(t^*), \widehat{w}(t^*) = w(t^*)$, and because $\Delta t_j = 0$ s in Eq. (10) it results in $t = t^*$, with Eq. (12) reducing to the conventional definition of the wind field: $u^{tot}(t) = U_j + u(t)$, $v^{tot}(t) = v(t)$ and $w^{tot}(t) = w(t)$.

4. Wind-vehicle-bridge interaction under skew winds

This section extends the wind-vehicle-bridge interaction (W-VBI) analysis framework presented in [5] to account for skew winds. The process starts with the definition of the bridge vibration properties and its environment, including the skew wind velocity field, the traffic conditions and the pavement irregularities. The vibration properties of the bridge are described with the frequencies of its relevant vibration modes (f) and with a mode matrix ($\mathbf{\Phi}$) that includes the corresponding mode shape vectors ($\boldsymbol{\phi}$). A large set of vibration modes are obtained from a finite element (FE) model of the structure, and the selection of those that are relevant to the dynamic response is usually based on the activated modal mass or the participation factors, or it can be done using more advanced techniques that also take into account the effect of the dynamic loading (see e.g. [18]). The skew wind speed time-histories at different points along the bridge are generated from the simulation process described in Section 2. The pavement irregularity profiles at the leeward and at the windward wheels of the vehicle are defined accounting for their transverse correlation as [19, 20]

$$r_L(x) = \sum_{m=1}^{N_n} \sqrt{2G_d(n_m)\Delta n} \cos(2\pi n_m x + \theta_m), \tag{15a}$$

$$r_W(x,y) = \sum_{m=1}^{N_n} \Bigg\{ \sqrt{2G_{d,x}(n_m,y)\Delta n} \cos\left(2\pi n_m x + \theta_m\right) + \sqrt{2\left[G_d(n_m) - G_{d,x}(n_m,y)\right]\Delta n} \cos\left(2\pi n_m x + \phi_m\right) \Bigg\}, \tag{15b}$$

in which r_L and r_W are the pavement irregularity profiles in the leeward and the windward wheel lines of the vehicle, respectively; N_n is the number of discrete spatial frequencies n_m included in the generation of these profiles, which are established between the lower and the upper cut-off frequency limits: $[n_1, n_{N_m}]$; Δn is the frequency resolution, in cycles/m; θ_m and ϕ_m are random phase angles uniformly distributed from 0 to 2π to generate a set of N_r independent profiles; $G_d(n_m)$ is the target one-sided PSD of displacements; and $G_{d,x}(n_m, y)$ is the one-sided cross PSD function [20], defined as

$$G_{d,x}(n_m) = \int_{-\infty}^{\infty} 2R(\sqrt{\delta^2 + 4b^2}) \exp^{i2\pi n_m \delta} \, \mathrm{d}\delta, \tag{16}$$

where R is the autocorrelation function of the displacement irregularity profile; δ is the longitudinal projection of the distance between two points in the pavement irregularity surface; b is the half-distance between the vehicle wheel lines in the transverse direction. The larger the value of b the more uncorrelated the profiles r_L and r_W are.

The coupled system of dynamics that governs the W-VBI problem is established in terms of the modal coordinates associated with the relevant vibration modes of the bridge ($\mathbf{q}_b$) and the displacement vector of the MDOF vehicle model ($\mathbf{q}_v$), as well as their time-derivatives

$$\begin{bmatrix} \mathbf{M}_b & \mathbf{0} \\ \mathbf{0} & \mathbf{M}_v \end{bmatrix} \begin{bmatrix} \ddot{\mathbf{q}}_b \\ \ddot{\mathbf{q}}_v \end{bmatrix} + \begin{bmatrix} \mathbf{C}_b & \mathbf{0} \\ \mathbf{0} & \mathbf{C}_v \end{bmatrix} \begin{bmatrix} \dot{\mathbf{q}}_b \\ \dot{\mathbf{q}}_v \end{bmatrix} + \begin{bmatrix} \mathbf{K}_b & \mathbf{0} \\ \mathbf{0} & \mathbf{K}_v \end{bmatrix} \begin{bmatrix} \mathbf{q}_b \\ \mathbf{q}_v \end{bmatrix} = \begin{bmatrix} \mathbf{\Phi}^{\mathrm{T}}(\mathbf{f}_{b,r} + \mathbf{f}_{b,w}) \\ \mathbf{f}_{v,g} + \mathbf{f}_{v,r} + \mathbf{f}_{v,w} \end{bmatrix}, \tag{17}$$

where $\mathbf{M}_v$, $\mathbf{C}_v$ and $\mathbf{K}_v$ are the mass, damping and stiffness matrices of the vehicle(s), respectively, with $\mathbf{M}_b$, $\mathbf{C}_b$ and $\mathbf{K}_b$ being the corresponding modal matrices of the bridge; $\mathbf{f}_{v,r}$ is the forcing vector at the vehicle wheels due to the moving wheel-pavement contact, including the effect of the pavement irregularities, with $\mathbf{f}_{b,r}$ being its counterpart in the bridge; $\mathbf{f}_{v,g}$ describes the gravity force in the vehicle and $\mathbf{f}_{v,w}$ the wind forces acting on it. The latter is composed of three forces and three moments applied on the vehicle as described in Eq. (1) based on a steady approach.

The forcing vector $\mathbf{f}_{b,w}$ represents the wind actions on the deck in each time-step of the analysis. The along-deck component (v^{tot}) is ignored in the direct wind forcing on the bridge due to its small influence in conventional structures with straight decks of reduced longitudinal slope. Consequently, the wind actions are applied on simplified models of the true cross-sections at each node of the deck with 3 degrees-of-freedom (DOF) each; this model includes the displacement in the direction perpendicular to the SP (p, across-deck), the vertical displacement (h, heave motion) and the torsional rotation of the deck (α). The generalised displacement vector at a particular node of the deck $[p, h, \alpha]^{\mathrm{T}}$ is associated with the wind actions $\mathbf{f}_{b,w} = [f^D_{b,w}, f^L_{b,w}, f^M_{b,w}]^{\mathrm{T}}$ that represent the drag, lift and moment components of the wind at that node, respectively. These forces are given by the linear superposition of the mean, buffeting and self-excited actions, that is: $\boldsymbol{f}_{b,w} = \boldsymbol{f}_{b,w-s} + \boldsymbol{f}_{b,w-b} + \boldsymbol{f}_{b,w-se}$.

The mean (quasi-static) wind forces in the structure are defined in terms of the along-flow mean wind speed projected in the transverse axis of the bridge ($\bar{U}_y$ defined in Eq. (14a)), and take the form

$$f^D_{b,w-s} = \frac{1}{2}\rho\bar{U}_y^2 D C^b_D \tag{18a}$$

$$f^L_{b,w-s} = \frac{1}{2}\rho\bar{U}_y^2 B C^b_L \tag{18b}$$

$$f^M_{b,w-s} = \frac{1}{2}\rho\bar{U}_y^2 B^2 C^b_M, \tag{18c}$$

where B and D are the width and the depth of the structural element, respectively; $C^b_D(\alpha_s)$, $C^b_L(\alpha_s)$ and $C^b_M(\alpha_s)$ are the drag, lift and moment aerodynamic coefficients of the structure for the angle of attack α_s, formed between the across-deck wind projection ($\bar{U}_y$) and the corresponding cross-section in static equilibrium.

There are different models in the literature to obtain the buffeting and the aeroelastic actions. For simplicity, these are calculated here with the linear quasi-steady (LQS) model [21] in which the fluid memory is neglected, and with it the aerodynamic admittance. Although the LQS effectively increases the buffeting forces, for the typical bluff sections in bridge decks the aerodynamic admittance can be ignored [22]. In addition, this work focuses on the interaction between vehicles and bridges, and Kavrakov *et al.* [23] demonstrated that the choice of the aerodynamic model does not strongly influence the W-VBI analysis for the wind speeds in which bridges are in operation, which are usually much lower than the design ones. Finally, Tang *et al.* [24] observed that flutter effects are reduced in bridges under skew winds. Accepting the LQS model, the buffeting forces are:

$$f^D_{b,w-b} = \frac{1}{2}\rho\bar{U}_y\left(2DC^b_D u + \left(DC^{b'}_D - BC^b_L\right)w\right) \tag{19a}$$

$$f^L_{b,w-b} = \frac{1}{2}\rho\bar{U}_y\left(2BC^b_L u + (BC^{b'}_L + DC^b_D)w\right) \tag{19b}$$

$$f^M_{b,w-b} = \frac{1}{2}\rho\bar{U}_y B^2\left(2C^b_M u + C^{b'}_M w\right), \tag{19c}$$

in which u and w are the across-deck and vertical turbulence components obtained from Section 2, respectively; $C^{b'}_D(\alpha_s)$, $C^{b'}_L(\alpha_s)$ and $C^{b'}_M(\alpha_s)$ are the angle-derivatives of the static wind coefficients at α_s. Finally, the self-excited forces are calculated with the LQS model:

$$f^D_{b,w-se} = \frac{1}{2}\rho\bar{U}_y\left(\bar{U}_y DC^{b'}_D\alpha - 2DC^b_D\dot{p} - \left(DC^{b'}_D - BC^b_L\right)\dot{h}\right) \tag{20a}$$

$$f^L_{b,w-se} = \frac{1}{2}\rho\bar{U}_y\left(\bar{U}_y BC^{b'}_L\alpha - 2BC^b_L\dot{p} - \left(BC^{b'}_L + DC^b_D\right)\dot{h}\right) \tag{20b}$$

$$f^M_{b,w-se} = \frac{1}{2}\rho\bar{U}_y B^2\left(\bar{U}_y C^{b'}_M\alpha - 2C^b_M\dot{p} - C^{b'}_M\dot{h}\right). \tag{20c}$$

It is noted that the width of the true (perpendicular) cross-section of the deck (B) is used instead of the along-flow deck width ($B/\sin(\beta)$), and the aerodynamic coefficients and their angle-derivatives also correspond to the orthogonal cross-section of the deck, unlike in the proposal of [6]. This is because the aerodynamic forces are based on the across-deck and vertical wind components (u and w, respectively) obtained in Eq. (13).

Finally, the W-VBI problem described in Eq. (17) is solved in the time-domain by the accelerated mode superposition algorithm included in the MDyn Python library [18].

5. Case study

5.1. Description of the structure, the FE model and the modal analysis

The proposed methodology is applied to the assessment of the driving accident risks in a 1287-m long bridge with a main span of 190 m. The elevation of the structure is shown in Fig. 6. The deck is composed of two 12-m wide prestressed concrete box girders with a variable depth ranging from 4 m at midspan and the approaching spans, to 12 m at the central piers (P9 and P10). Fig. 7 presents the cross-sections of the deck at these positions, including two 1.7-m high edge barriers that run along the entire length of the deck. The deck also has a variable height from the ground (z_j) and it is highest at midspan in the central span (48.1 m above the river). This is considered in the generation of the wind field from a target boundary layer profile, but the slope of the deck is ignored in the calculation of the aerodynamic wind actions and the dynamic response of the vehicle. The deck is straight in plan and its centreline forms the vertical SP.

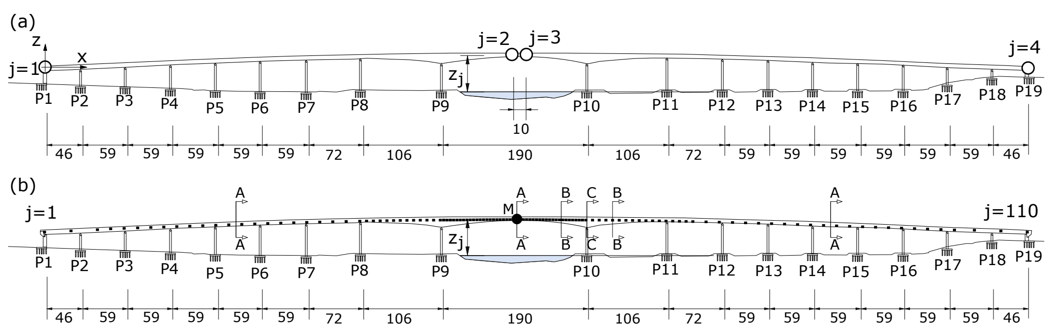

Figure 6: Elevation of the bridge and position of the nodes where wind is generated; (a) simplified case with $N_p = 4$ nodes, (b) proposal with $N_p = 110$ nodes used for the full simulation. Units in meters.

The deck of the bridge is modelled in the FE analysis software package ABAQUS [25] using two separate lines of linear-interpolation 3D beam elements connecting the centroids of each box girder. A total of 2600 elements are used to discretise the deck, with a typical length of 1 m to capture accurately the variation of its depth. The mass of the asphalt is introduced by increasing the density of the concrete in the deck, whilst the parapets, sidewalks, barriers and diaphragms are included as lumped masses positioned at their corresponding centroids. The piers are modelled with the same type of beam elements as the deck and they are fully fixed to the ground. The deck

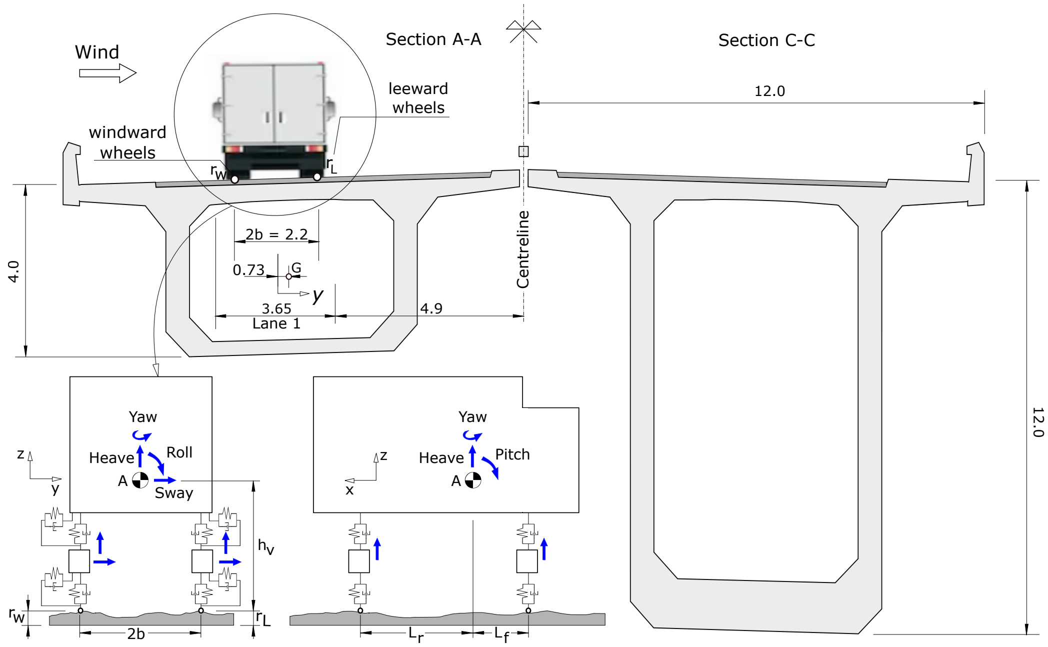

Figure 7: Typical cross-sections of the deck and detail of the application of the irregularity profiles (r_W, r_L) to the vehicle wheels. The numerical model of the vehicle and its DOF are included. Units in m.

is pinned to the piers by means of support devices that allow the longitudinal movement (in the x direction) at all the supports with the exception of piers P8 to P14, where it is fixed. The FE model of the bridge has approximately 16000 DOFs.

A modal analysis was conducted in this model to obtain the most relevant vibration modes of the bridge for the W-VBI problem. The first mode with lateral movement of the deck has a frequency of 0.5 Hz and it involves the main span and the two adjacent spans (P8-P11). The first mode with vertical movement of the deck also involves these spans and has a frequency of 0.77 Hz. A sensitivity analysis showed that the lateral and vertical modes above 5 Hz can be ignored, which lead to include a total of 74 vibration modes in the dynamic analysis of the bridge.

5.2. Simulation of non-orthogonal wind fields

The methodology described previously to simulate both orthogonal non-orthogonal wind velocity signals is applied to generate 3D wind fields at the centreline of the bridge deck. The GP is defined as the vertical plane that forms an angle β with the normal of the SP and intersects with it at the left abutment (P1) if $\beta < 90°$, or at the right abutment (P19) if $\beta > 90°$. The time-step and the frequency band width considered in the wind field generation are $\Delta t = 0.01$ s and $\Delta f = 0.001$ Hz, respectively. The along-flow mean wind speed profile is defined ignoring orographic effects and considering the specifications of EN1991-1-4 [26] and the UK recommendations [27, 28] for terrain Type II, regardless of the wind incidence angle:

$$\widehat{U}_j = 0.19\log\left(\frac{z_j}{0.05}\right)\widehat{U}_{z,10}, \tag{21}$$

where z_j is the height above ground of the j-th node and $\widehat{U}_{z,10}$ is the mean along-flow wind speed at $z = 10$ m. The height z_j is conservatively measured from the level of the free surface of the river in Fig. 6. For convenience, the reference mean wind speed is taken at the lowest point of the deck (P19, where $z = 29.5$ m) and it is referred to as $\widehat{U}_b$. Therefore, $\widehat{U}_{z,10} = \widehat{U}_b/(0.19\log(29.5/0.05)) = 0.82\widehat{U}_b$. The along-flow turbulence intensity also depends on z_j but it is considered independent of the wind incidence angle

$$I_j^{\widehat{u}} = \frac{1}{\log\left(\frac{z_j}{0.05}\right)}, \tag{22}$$

which leads to values of $I_j^{\widehat{u}} \approx 0.15$ along the deck of the bridge. According to [29] and assuming that the terrain is homogeneous the across-flow turbulence intensities are taken as: $I_j^{\widehat{v}} = 0.75 I_j^{\widehat{u}} \approx 0.11$ and $I_j^{\widehat{w}} = 0.5 I_j^{\widehat{u}} \approx 0.075$. The along-flow turbulence length scale is estimated from EN 1991-1-4 [26] as $L^{\widehat{u}} = 139$ m. The turbulence lengths in the longitudinal and vertical directions are obtained as: $L^{\widehat{v}} = 0.25 L^{\widehat{u}} \approx 34.75$ m and $L^{\widehat{w}} = 0.1 L^{\widehat{u}} \approx 13.9$ m, respectively. This allows to define the frequency content of the turbulence with the Kaimal spectra as

$$\frac{f \widehat{G}^i_{jj}(f)}{(\sigma^i_j)^2} = \frac{A^i \tilde{f}^i}{(1 + 1.5 A^i \tilde{f}^i)^{5/3}}, \tag{23}$$

where $\sigma^i_j = I^i_j \widehat{U}_j$ is the standard deviation of the turbulence in the i-th direction and the j-th node of the GP, with $i = \widehat{u}, \widehat{v}, \widehat{w}$. The Kaimal spectra are given in terms of the reduced frequency $\tilde{f} = f L^i / \widehat{U}_j$ using the parameters $A^{\widehat{u}} = 6.8$ and $A^{\widehat{v}} = A^{\widehat{w}} = 9.4$. Fig. 8 shows the resulting spectra referred to the GP axes.

In order to illustrate the simulation process the wind time-history signals are generated first at only four nodes of the bridge deck ($j = 1 - 4$), as described in Fig. 6(a). These include the two abutments, and also two points closely spaced at the central span to study the spatial coherence properties of the simulated wind histories. The (x, z) coordinates of the four nodes with respect to the SP axes are as follows: node 1 (0, 31.9) m, node 2 (619.5, 48.1) m, node 3 (629.5, 48.1) m and node 4 (1307, 29.5) m. Fig. 8 shows the reduced auto-spectral density of the generated wind signals for one of the records at the midspan node $j = 2$ in Fig. 6(a), with $\beta = 90°$ and $U_b = 20$ m/s. The Root Mean Square (RMS) of the spectra obtained from the signals is also presented to reduce the frequency-to-frequency variability and facilitate comparison [30]

$$\widehat{G}^i_{jj,\mathrm{RMS}}(\tilde{f}) = \sqrt{\frac{1}{\Delta \tilde{f}_{\mathrm{RMS}}} \int_{\tilde{f}+\Delta \tilde{f}_{\mathrm{RMS}}/2}^{\tilde{f}-\Delta \tilde{f}_{\mathrm{RMS}}/2} (\widehat{G}^i_{jj}(\tau))^2 \,\mathrm{d}\tau}, \tag{24}$$

in which $\Delta \tilde{f}_{\mathrm{RMS}} = 1$ is the window width in the RMS average. The results indicate that the single-point frequency content of the generated signals is close to the target in the GP.

The first 60 s of the along-flow and across-deck wind velocity signals at midspan ($j = 2$) are included in Fig. 9 for three different incidence angles.

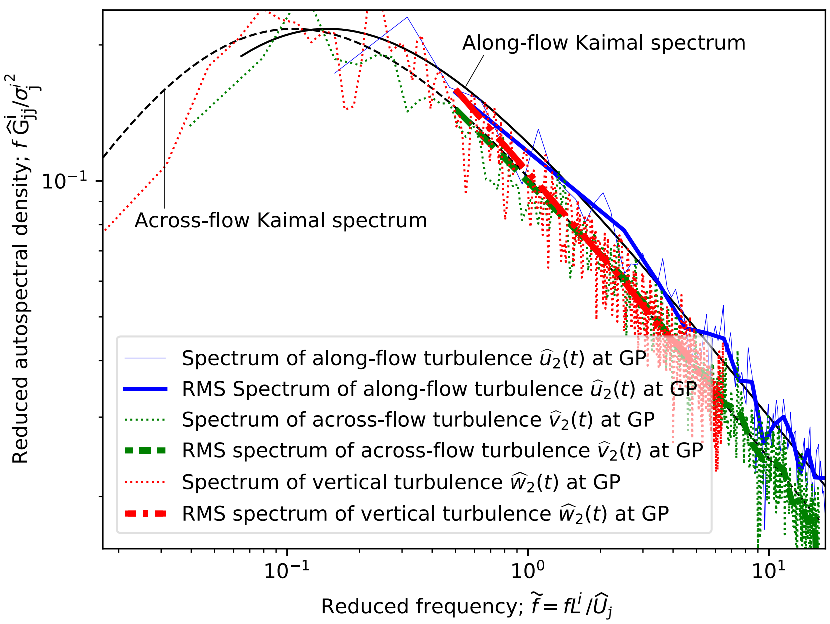

Figure 8: Kaimal spectra in the along- and across-flow directions at the GP compared with the ones resulting from the simulation at midspan ($j = 2$) when $\beta = 90°$. $\widehat{U}_b = 20$ m/s. Sample Record #1.

In order to facilitate comparison, the same set of random numbers θ_{km} are considered for the three wind directions (although they are different for the three components of the wind turbulence). Purely cross-winds ($\beta = 90°$) have no time-lag ($\Delta t_2 = 0$ s) associated and the wind speed history obtained at the GP is identical to that at the SP (Fig. 9(b)). However, if $\beta = 45°$ the reference node is at the left abutment ($r = 1$) and the time-lags at the four nodes are $\Delta t_j = 0, 20.3, 20.6, 49.0$ s with $j = 1, 2, 3, 4$, respectively. Fig. 9(a) shows the time-lag at midspan and how the process of removing this interval and rotating the signal to the SP changes the wind time-history significantly compared with the purely cross-wind, reducing its mean in the across-deck direction ($\bar{U}_{y,j}$). When $\beta = 135°$ the rotated across-deck velocity signal is also reduced remarkably, in this case the reference node is at the right abutment ($r = 4$) and the time-lags for the four nodes are $\Delta t_j = 48.5, 25.2, 24.8, 0$ s. It is noted that the two non-orthogonal wind incidence angles proposed lead to GPs that are symmetric with respect to the center of the bridge, but there are small differences in the time-lags at the abutment opposite to the referene node: $\max(\Delta t_j) = 49$ s and 48.5 s for $\beta = 45°$ and 135°, respectively. This is because the two abutments have different heights and therefore different mean wind speeds.

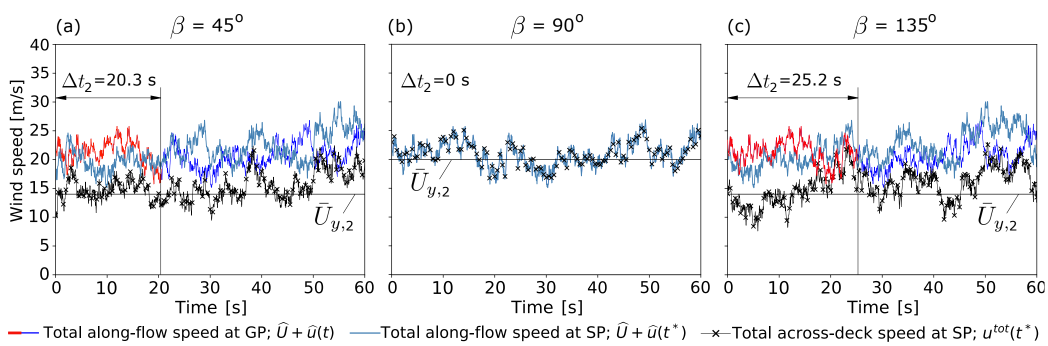

Figure 9: Wind velocity history at midspan ($j = 2$) and its projection in the GP for wind incidence angles: (a) $\beta = 45°$, (b) $\beta = 90°$ and (c) $\beta = 135°$. $\widehat{U}_b = 20$ m/s. Sample Record #1.

The frequency content of the wind velocity records presented in Fig. 9 is included in Fig. 10, excluding the along- and across-flow signals at the SP because their spectra coincide exactly with that of the time-histories at the GP. When $\beta = 90°$ the generated velocity time-histories match very well the target Kaimal spectra in all the directions, as shown in Fig. 8, with identical results in the GP and in the SP. If $\beta \neq 90^\circ$ the signals at the GP also match the correspoding target spectra but after rotating them to align with the SP their frequency content changes. This is because the across- and along-deck signals at the SP result from the contribution of the instantaneous along- and across-flow time-histories when the wind is non-orthogonal to the deck. In this case the reduced spectra cannot be obtained from the wind properties of a single wind direction. For this reason the arithmetic mean of the along- and across-flow turbulence length scales and intensities are considered in Fig. 10 when $\beta = 45^\circ$ and $\beta = 135^\circ$. The spectra of the vertical wind speed is not affected by β, as it results from Eq. (12c).

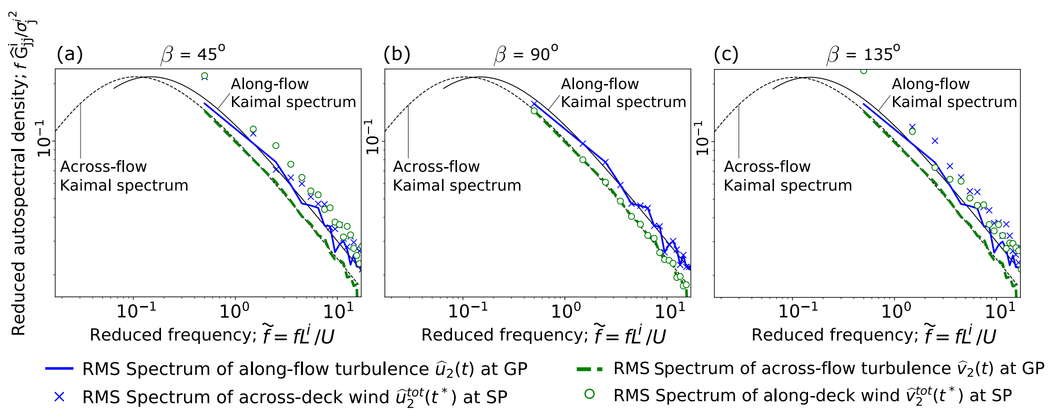

Figure 10: Reduced autospectra of the wind velocity histories at midspan ($j = 2$) and its projection in the GP for wind incidence angles: (a) $\beta = 45^\circ$, (b) $\beta = 90^\circ$ and (c) $\beta = 135^\circ$. $\widehat{U}_b = 20$ m/s. Sample Record #1.

After exploring the time-histories and the frequency content of the wind generated at one point of the bridge ($j = 2$), the spatial correlations of the signals at the four nodes described in Fig. 6(a) are considered. The spatial coherence decrements of the wind at the bridge site are taken from the work of Solari and Piccardo [31] as $C^{\widehat{u}}_{\widehat{x}} = C^{\widehat{u}}_{\widehat{z}} = 10$ for the along-flow turbulence, $C^{\widehat{v}}_{\widehat{x}} = C^{\widehat{v}}_{\widehat{z}} = 6.5$ for the across-flow horizontal turbulence, and $C^{\widehat{w}}_{\widehat{x}} = 6.5$ and $C^{\widehat{w}}_{\widehat{z}} = 3$ for the vertical turbulence. Fig. 11 includes the total (mean plus turbulence) wind velocity histories at the four nodes for the three incidence angles. The results refer to the axes of the SP. The wind incidence angle (β) affects slightly the vertical wind time-histories because of the time-lags between the GP and SP. However, β affects the other two components of the wind signals more significantly. The across-deck wind speed is maximised for pure cross-winds, reaching a mean value that coincides with that corresponding to the along-flow wind profile obtained from Eq. (21). On the other hand, the magnitude of the along-deck wind component increases significantly under non-orthogonal winds, giving positive values when $\beta < 90°$ and negative when $\beta < 90°$. This has a large influence in the driving safety when combined with the speed of the vehicles, as it will be discussed in Section 6. It has also been observed that the mean values of the total across- and along-deck wind velocity signals satisfy the 'cosine' rule and therefore verify Eq. (14):

$$\mathrm{E}(u_j^{tot}(t^*)) = \bar{U}_{y,j} = \widehat{U}_j \sin(\beta) \tag{25a}$$

$$\mathrm{E}(v_j^{tot}(t^*)) = \bar{U}_{x,j} = \widehat{U}_j \cos(\beta), \tag{25b}$$

with $\mathrm{E}(\cdot)$ representing the expected value of its argument.

In all the cases it is observed that the wind signals at the two abutments ($j = 1$ and $j = 4$) are very uncorrelated due to the large distance between them (approximately 1300 m), but those at the two points spaced 10 m at midspan ($j = 2$ and $j = 3$) are more similar, particularly the more skew is the wind incidence angle with respect to the bridge. This is further explored in Fig. 12 by plotting the spatial coherence between the wind histories at points $j = 2$ and $j = 3$ for a wide range of vibration frequencies obtained from the rearrangement of Eq. (7) as

$$\widehat{\gamma}_{jk}^{i}(f_m) = \frac{\widehat{G}_{jk}^{i}(f_m)}{\sqrt{\widehat{G}_{jj}^{i}(f_m)\widehat{G}_{kk}^{i}(f_m)}}. \tag{26}$$

The target coherence function ($\widehat{\gamma}$) in Fig. 12 is obtained from Eq. (8), and it is compared with the standard non-projected function γ that results by introducing $\beta = 90°$ in this equation. For pure cross-winds the two functions are identical and the generated signals match the coherence decrement well. If $\beta \neq 90°$ the projected points of the structure in the GP are closer to each other than in the SP, which increases the coherence function ($\widehat{\gamma} > \gamma$) for any f. This is in agreement with Xie *et al.* [12], who found that larger skew angles increase the magnitude of the integral of coherence slightly. Fig. 12 also shows that the coherence of the non-orthogonal signals in the GP follows the target $\widehat{\gamma}$, however, the coherence of the rotated wind histories in the SP is slightly different due to the contribution of the along- and across-flow components.

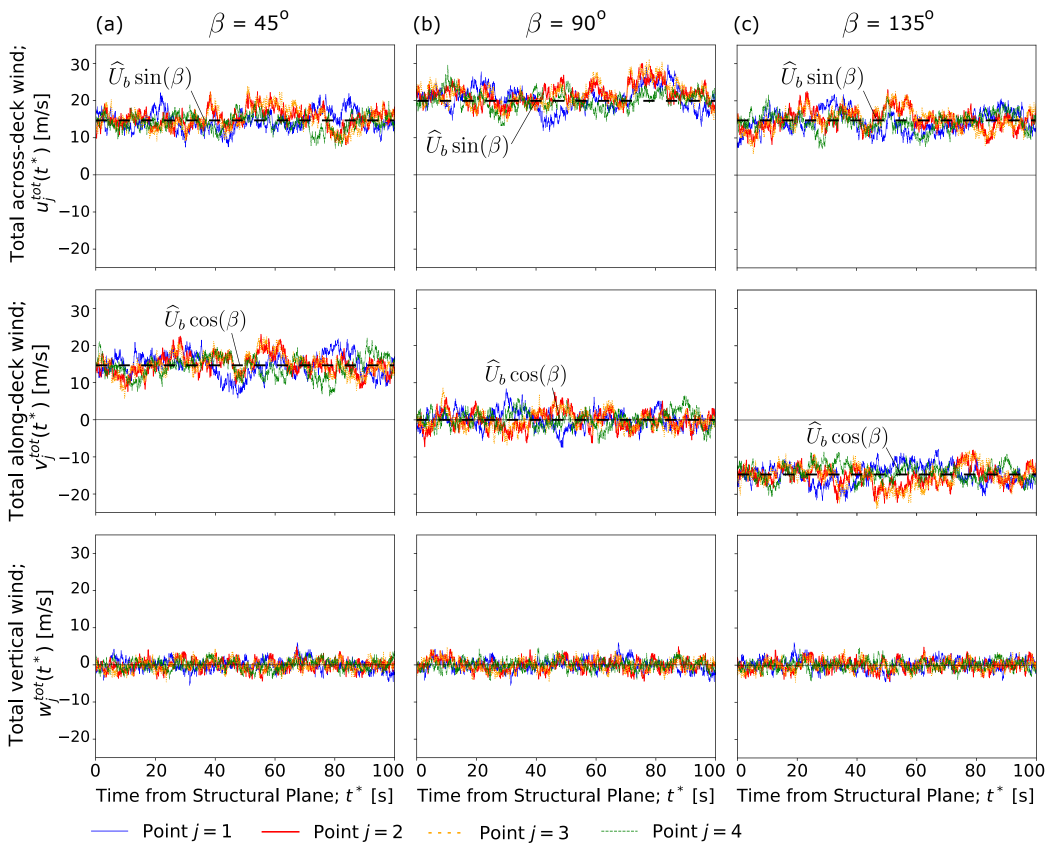

Figure 11: Total wind speed along the three axes of the SP for wind incidence angles: (a) $\beta = 45°$, (b) $\beta = 90°$ and (c) $\beta = 135°$. $\widehat{U}_b = 20$ m/s. Sample Record #1.

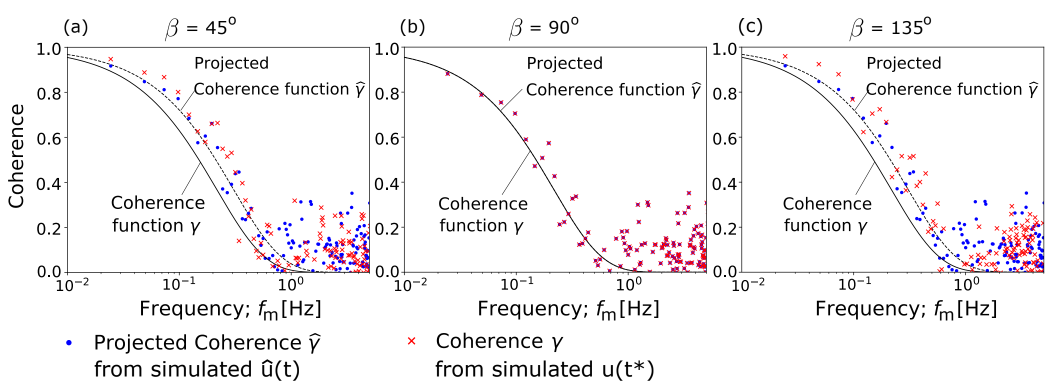

Figure 12: Spatial coherence in the along-flow ($\widehat{u}(t)$) and across-deck ($u(t^*)$) signals at the points $j = 2$ and $j = 3$ of the deck: (a) $\beta = 45°$, (b) $\beta = 90°$ and (c) $\beta = 135°$. $\widehat{U}_b = 20$ m/s. Sample Record #1.

For the subsequent assessment of the bridge and the vehicle responses under skew winds a more complete definition of the wind field in $N_p = 110$ nodes of the deck is proposed, as shown in Fig. 6(b). These points are concentrated in the central span, where the vibration of the deck and the along-flow mean wind speeds are larger. The duration of the wind signals generated in the GP is 600 s. This results in shorter signals at the SP due to Δt_j, reaching a minimum of 551 s for $\beta = 45°$ or 135°. In the following, the same set of random phase angles are used in the wind simulation regardless of the skew angle to facilitate comparison between the results obtained for different values of β.

5.3. Response of the bridge without vehicles

The response of the bridge under wind actions with different incidence angles and without vehicles is considered first using the LQS model in MDyn. A fixed time-step of 0.01 s and a damping ratio $\xi = 1\%$ equal for all the vibration modes are used in the analysis. The wind speed is increased linearly from zero to its full value in the first 10 seconds of the dynamic analysis to avoid introducing unrealistic wind-induced impacts in the structure. In the following, the basic wind speed is $\widehat{U}_b = 22.35$ m/s (50 mph).

The DOFs corresponding to the downwind girder and to the piers are deactivated in the LQS analysis to reduce the computational time [18]. Although the wind actions are only applied in the upwind girder, the effect of the downwind box in the wind flow is included through the aerodynamic coefficients of the deck (C_D^b, C_L^b, C_M^b) and their angle-derivatives $(C_D^{b'}, C_L^{b'}, C_M^{b'})$. These were obtained from two-dimensional computational fluid dynamic (CFD) simulations of the wind flow around the bridge deck sections conducted in ANSYS Fluent [32] for angles of attack of the wind with respect to the transverse axis of the structure (y) ranging from $\alpha_s = -10°$ to 10°. The CFD analysis was conducted using the SST $k-\omega$ turbulence model with an initial time-step of 5×10^{-5} s and a thickness of the first layer of elements next to the walls of the deck of 1.25 mm. The variable shape of the deck is considered in MDyn by introducing the aerodynamic properties of three different cross-sections analysed in the CFD model, as shown in Fig. 6(b): Section A at midspan, Section C at the supports with the main piers (P9 and P10), and Section B at an intermediate position between the other two.

Fig. 13 presents the time-histories of the wind-induced movements at midspan (point M in Fig. 6(b)) for one of the generated wind records. It is observed that the transverse displacement of the deck (r_y) is larger than the vertical one (r_z), particularly for purely cross-winds because the quasi-static effects of the mean wind acting on the deck are maximised. However, the dynamic movement of the deck in the vertical direction is also influenced by the wind skew angle β, even though the mean value of the vertical wind velocity signals is unaltered. This is because the buffeting and the aeroelastic lift forces in Eqs. (19b) and (20b) are also affected by the across-deck mean wind speed and turbulence ($\bar{U}_{y,j}$ and $u(t^*)$), as well as by the lateral velocity of the deck ($\dot{p}$), which depend on β.

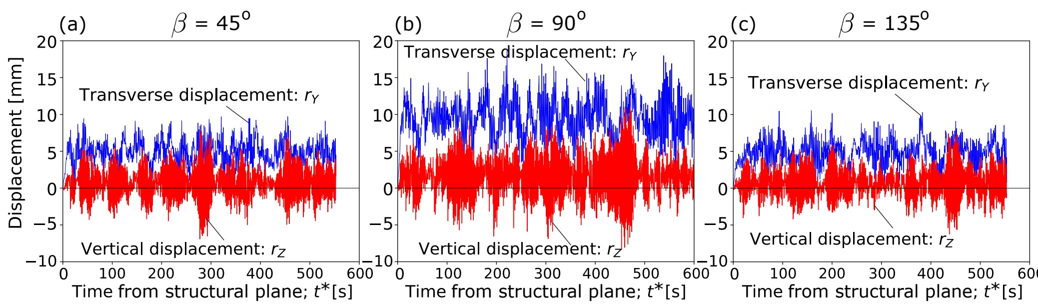

Figure 13: Time-history of the bridge displacement at midspan without vehicle: (a) $\beta = 45°$, (b) $\beta = 90°$ and (c) $\beta = 135°$. $\widehat{U}_b = 22.35$ m/s; Sample Record #1.

The peak displacements of all the nodes along the upwind girder of the bridge are presented in Fig. 14. The lines in the plots refer to the arithmetic mean of 10 independent wind records, and the width of the colour bands centered around them indicates the mean plus and minus one standard deviation. The larger influence of β in the transverse response is observed along the deck, and particularly at the main span. In this region, purely cross-winds also maximise the vertical movements and their dispersion for different records. This is due to the higher mean wind speed at midspan and, especially, due to the larger flexibility of the deck in this region. The main piers P9 and P10 are much stiffer than the rest in the lateral direction, and for this reason the transverse displacements of the deck at these points is very small compared with those at the intermediate piers.

5.4. Aerodynamic effects on the vehicles crossing the bridge

This part of the study focuses on the influence of skew winds on the W-VBI problem, considering a single high-sided vehicle crossing the bridge in the negative-x direction (i.e. from P19 to P1) at a constant speed of $V_d = -64.4$

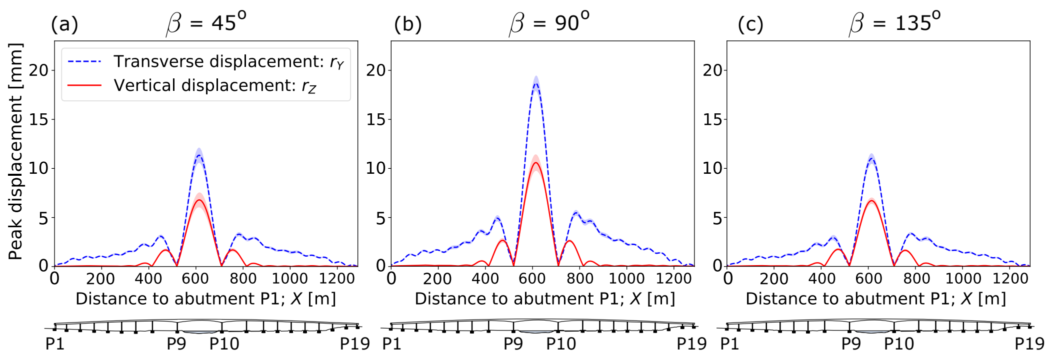

Figure 14: Peak displacement along the deck for 10 different records: (a) $\beta = 45°$, (b) $\beta = 90°$ and (c) $\beta = 135°$. No vehicle; $\widehat{U}_b = 22.35$ m/s. The thick lines represent the mean values and the total width of the colour bands indicates two standard deviations.

km/h (-40 mph). The vehicle is modelled as a 13-DOF system represented in Fig. 7, which includes heave, sway, roll, pitch and yaw of the vehicle box, and vertical and lateral displacements of its four wheel/suspension masses. The mechanical properties of the vehicle are adapted from Xu and Guo [2], and they are included in Table 1. The vehicle follows a straight path on the upwind girder with an eccentricity of 0.73 m between their centroids (see Fig. 7). The wind velocity histories acting on the vehicle are obtained by linear interpolation between the two nodes of the deck (or the approaching platforms) that are adjacent to the vehicle centroid at each time-step of the analysis. The wind velocity on the vehicle is increased linearly when it is on the approaching platform, ranging from 0 at the start of the analysis to full wind speed when the front wheels access the deck of the bridge (at this instant the deck is also subject to full wind speed). This is to avoid introducing unrealistic transient dynamic effects on the vehicle.

The pavement irregularities are generaged in the bridge and in the approaching platforms according to the target PSD given in ISO 8608 [33]

$$G_d(n) = G_d(n_0)\left(\frac{n}{n_0}\right)^{-2}, \tag{27}$$

where $n_0 = 0.1$ cycles/m is a reference frequency and $G_d(n_0) = 16 \times 10^{-6}$ m^3/cycle defines a road with 'very good quality' (Category A) according to [33]. The pavement profiles in Eq. (15) are generated each 0.01 m and contain spatial frequencies ranging from $n_1 = 6.3 \times 10^{-4}$ cycles/m (lower bound) to $n_{N_m} = 20$ cycles/m (upper bound), with a resolution of $\Delta n = 1.0 \times 10^{-4}$

Parameter	Units	Value
Full length of the vehicle	m	13.45
Longitudinal distance from centroid to front wheels (L_f)	m	3
Longitudinal distance from centroid to rear wheels (L_r)	m	5
Reference (front) area (A_v)	m^2	10.5
Vertical distance between wheels and centroid (h_v)	m	1.0
Half-distance between wheel lines (b)	m	1.1
Vertical distance between upper suspension and centroid	m	0.8
Mass of the vehicle body	kg	4480
Pitching moment of inertia of vehicle body	kg·m^2	5516
Rolling moment of inertia of vehicle body	kg·m^2	1349
Yawing moment of inertia of vehicle body	kg·m^2	100000
Mass of each wheel in front axle	kg	800
Mass of each wheel in rear axle	kg	710
Upper vertical spring stiffness (all wheels)	kN/m	399
Upper lateral spring stiffness (all wheels)	kN/m	299
Upper vertical damper coefficient in front wheels	kN·s/m	23.21
Upper lateral damper coefficient in front wheels	kN·s/m	23.21
Upper vertical damper coefficient in rear wheels	kN·s/m	5.18
Upper lateral damper coefficient in rear wheels	kN·s/m	5.18
Lower vertical spring stiffness (all wheels)	kN/m	351
Lower lateral spring stiffness (all wheels)	kN/m	121
Lower vertical damper coefficient (all wheels)	kN·s/m	0.8
Lower lateral damper coefficient (all wheels)	kN·s/m	0.8

Table 1: Mechanical properties of the vehicle considered in this study. Adapted from [2].

cycles/m. The transverse and the longitudinal slopes of the deck are ignored in the simulation of the pavement irregularities, as well as their discontinuities at the bridge joints in P1 and P19.

Fig. 15 presents different parameters that are representative of the wind actions and the response of the vehicle as it crosses the bridge for different skew angles, considering a particular wind record and pavement profile. The instantaneous values of the relative wind incidence angle on the vehicle ($\psi(x, t^*)$) are shown in Figs. 15(a-c). These are obtained by introducing in Eq. (4) the total wind time-histories obtained from Eq. (12) (mean plus turbulence). In addition, the mean vales of the relative incidence angle ($\bar{\psi}(x)$) are given by ignoring the turbulence components in Eq. (12) (i.e.

$\widehat{u}(t^*) = \widehat{v}(t^*) = 0$). It is noted that $\bar{\psi}$ depends on the vehicle position in the deck because the mean along-flow wind speed is higher in the central span. This is reflected in the curved shape of $\bar{\psi}$ in Figs. 15(a-c), which also shows that the instantaneous incidence angle oscillates from the mean value due to the wind turbulence. The skew angle of the wind (β) affects significantly the mean relative incidence angle on the vehicle, which is close to the critical value that maximises the aerodynamic coefficients of the vehicle ($\psi = 90°$) when $\beta = 135°$ (tailwind), as it was illustrated in Fig. 3(b). In addition, the instantaneous value of ψ is more sensitive to the wind turbulence when $\beta = 135°$, resulting in higher oscillations with respect to $\bar{\psi}$. However, Figs. 15(d-f) indicate that the effect of β on the relative wind speed (U_r) is opposite; U_r strongly increases with low skew angles (headwinds). The instantaneous value of the relative wind speed on the vehicle ($U_r(x,t)$) in Fig. 15(d) is obtained by introducing the turbulent wind record in Eq. (3), and it is approximately two times larger than the vehicle speed and the mean along-flow wind speed with $\beta = 45°$. As the skew angle of the wind increases the mean relative wind speed on the vehicle ($\bar{U}_r(x)$) decreases, taking values that are below the mean wind and driving speeds for $\beta = 135°$ (Fig. 15(f)). The wind turbulence is responsible for significant deviations of the instantaneous relative wind speed on the vehicle ($U_r(x,t)$) with respect to the corresponding mean value ($\bar{U}_r(x)$) as it crosses the bridge, particularly for tailwinds $\beta = 135°$ in which the difference can reach 50%.

Figs. 15(g-i) include the transverse wheel forces ($F_{c,Y}$) in the front and the rear axles of the vehicle (sum of the two wheel forces in each axle). The plots also represent the mean value of the side wind force on the vehicle ($\bar{f}^S_{v,w}$), which is non-uniform along the deck due to its variable height (z_j) and it is maximised at the main span. The value of $\bar{f}^S_{v,w}$ is obtained from Eq. (1a) by neglecting the turbulence of the wind, and it is divided over two in these figures to represent an ideal equal distribution of the side force on the two axles of the vehicle. This would occur if the two axles were at the same distance with respect to the point of application of the wind actions on the vehicle (Point A in Fig. 7), however, it can be observed that the front wheels transmit larger side forces to the pavement because they are closer to the centroid than the rear wheels in the proposed vehicle ($L_r = 5$ m $> L_f = 3$ m). The instantaneous side forces at both vehicle axles oscillates significantly due to the wind turbulence, particularly under tailwind conditions with $\beta = 135°$ for which the peak values can be up to four times larger than the mean of the corresponding axle side force (see Fig.

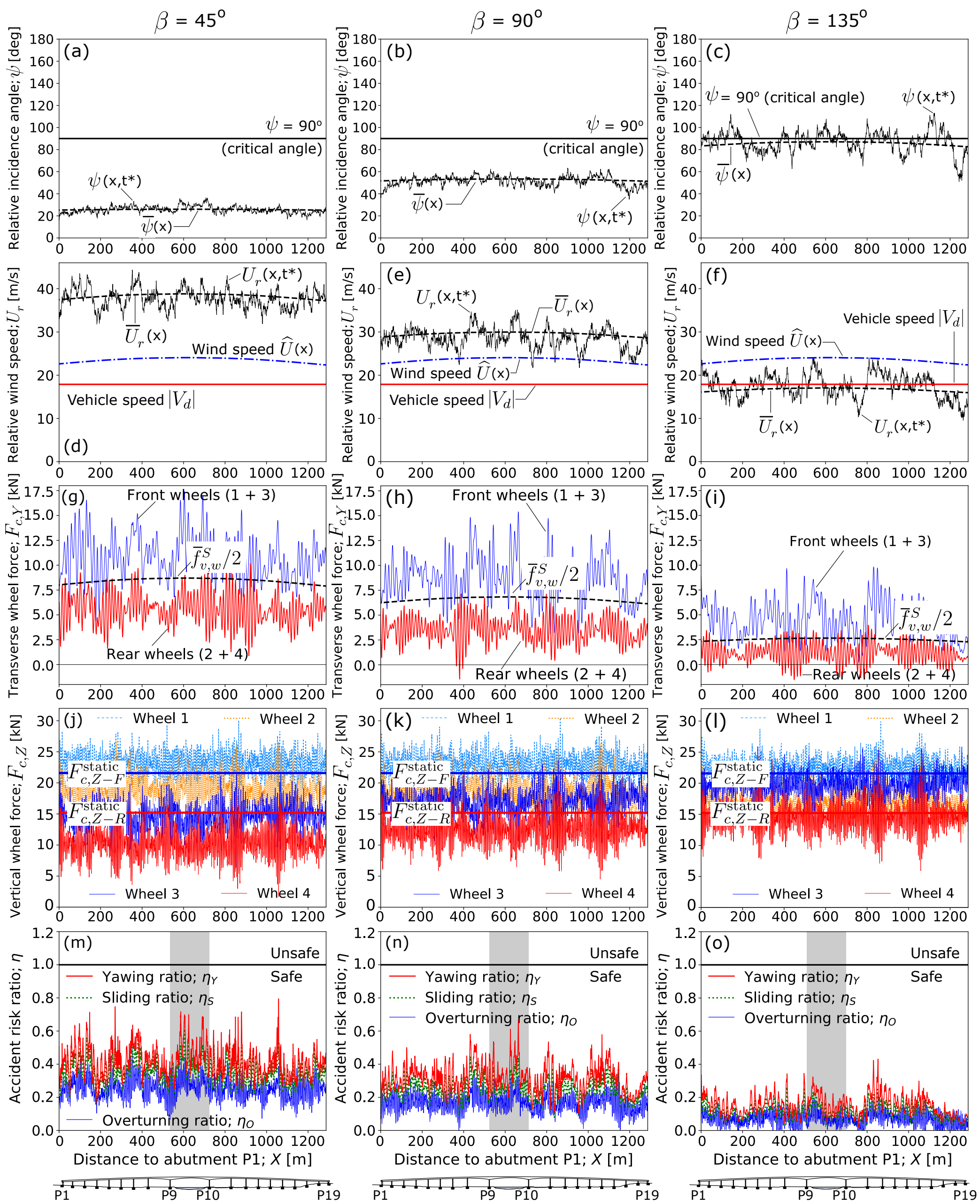

Figure 15: Actions on and response of the vehicle for three different apparent wind incidence angles β; (a-c) relative wind incidence angle on the vehicle ψ; (d-f) relative wind speed on the vehicle U_r; (g-i) transverse wheel forces $F_{c,Y}$; (j-l) vertical wheel forces $F_{c,Z}$; (m-o) accident risk ratios η, with the shaded band representing the region that corresponds to the main span of the bridge. $\widehat{U}_b = 22.35$ m/s; $V_d = -64.4$ km/h. Sample Record #1.

15(i)). Nevertheless, the side forces on the vehicle wheels can be significantly larger under headwind conditions, reaching peak values with $\beta = 45°$ that are 15% and 70% higher than in the analysis of the same record with $\beta = 90°$ and 135°, respectively. This is because the aerodynamic wind forces on the vehicle depend on the square of the relative wind speed, which makes them more sensitive to U_r than to ψ, as it was observed in Section 2.

The larger wind-induced side forces and rolling moments in the vehicle for $\beta = 45°$ explains the lower vertical tyre forces ($F_{c,Y}$) in its windward wheels (numbers 3 and 4 in Fig. 2(b)). This increases the risk of instantaneous wheel detachments from the road, although they are not observed for the studied record because $F_{c,Z} > 0$ at all times. The risk is highest at the rear windward wheel (number 4) because it is further from the centroid of the vehicle and hence the wheels in the rear axle carry a lower vertical static load ($F^{\text{static}}_{c,Z-R}$) than those in the front one ($F^{\text{static}}_{c,Z-F}$). The minimum vertical force in wheel 4 when $\beta = 45°$ is approximately 60% and 70% smaller than that observed for $\beta = 90°$ and 135°, respectively, considering the particular record studied in Fig. 15. It is also noted that the pavement irregularities are responsible for the high-order frequency of oscillation in the instantaneous vertical wheel forces, increasing significantly the risk of vehicle accidents, as it will be discussed in the next section.

6. Effects of the wind incidence angle on the driving accident risks

The driving accident risks are calculated from the time-histories of the vehicle wheel reactions in the vertical and the transverse directions: $F_{c,Z-wh}(t^*)$ and $F_{c,Y-wh}(t^*)$, respectively, with $wh = 1, \cdots, 4$ representing the wheel number included in Fig. 2. The accident risks are expressed as ratios in the form

$$\eta_o = \max_{t^*} \left[\frac{F_{c,Z-L}(t^*) - F_{c,Z-W}(t^*)}{F_{c,Z-L}(t^*) + F_{c,Z-W}(t^*)} \right] \tag{28a}$$

$$\eta_s = \max_{t^*} \left[\frac{|f^S_{v,w}(t^*)|}{\mu_c (F_{c,Z-F}(t^*) + F_{c,Z-R}(t^*))} \right] \tag{28b}$$

$$\eta_y = \max \left[\max_{t^*} \left(\frac{|F_{c,Y-F}(t^*)|}{\mu_c F_{c,Z-F}(t^*)} \right), \max_{t^*} \left(\frac{|F_{c,Y-R}(t^*)|}{\mu_c F_{c,Z-R}(t^*)} \right) \right]. \tag{28c}$$

in which η_o, η_s and η_y indicate, respectively, overturning, side-slipping and yawing vehicle accidents when they are above 1; $F_{c,Z-L} = F_{c,Z-1} + F_{c,Z-2}$ is the total vertical force in the leeward wheel line of the vehicle according to the wheel numbering in Fig. 2(b); $F_{c,Z-W} = F_{c,Z-3} + F_{c,Z-4}$ is the vertical force in the windward wheels; $F_{c,i-F} = F_{c,i-1} + F_{c,i-3}$ and $F_{c,i-R} = F_{c,i-2} + F_{c,i-4}$ refer to the total wheel forces at the front and rear wheel axles, respectively, with $i = Y, Z$ referring to the lateral and the vertical directions; μ_c is the tyre-pavement contact adherence. In this work a value of $\mu_c = 0.7$ is adopted to represent dry/moderately wet pavements [34].

Figs. 15(m-o) present the instantaneous values of the driving accident risks as the vehicle crosses the bridge for three different wind incidence angles, considering a particular pavement and wind record. Although accidents are not observed in this record, the risk is significantly higher under headwinds ($\beta = 45°$) than for purely cross-winds ($\beta = 90°$) and, particularly, for tailwinds ($\beta = 135°$). This is explained by the larger relative wind speed acting on the vehicle when $\beta = 45°$. In this study the driving instability risks are dominated by the side-slipping of the rear wheels and the consequent vehicle yawing because its centroid is relatively low and close to the front wheel axle. Yawing and side-slipping accident risk ratios peak when the vehicle is located at the main span of the bridge under cross-winds (Fig. 15(n)). This is because of the larger lateral wind-induced movements of the deck for $\beta = 90°$, as shown in Fig. 14. Under non-orthogonal wind directions the movement of the deck is significantly smaller and with it also the vehicle-bridge interaction, which leads to peak driving instability risks that can be maximised at any position along the bridge. This suggests that in skew wind conditions the lateral and vertical vibrations coming from the deck have smaller influence in the dynamic response of the vehicle than the direct actions (namely the pavement irregularities and the turbulent wind speed on the vehicle).

The influence of the skew angle in the W-VBI analysis is examined further by considering 19 different values of β ranging from 20° to 160°. The analysis is repeated for 10 different records of wind time-histories and pavement profiles in order to obtain statistically meaningful results of the driving accident risks according to [5]. The peak accident risk ratios obtained for each angle and record are shown in Fig. 16(a), with the thick lines representing the arithmetic mean of each type of accident and the width of the colour bands one standard deviation above and below the mean. The results indicate that headwinds acting on the vehicle are significantly more dangerous for its safety because of the increase of U_r, but very inclined winds with small values of β compensate this effect by reducing significantly the relative incidence angle ψ and, hence, the aerodynamic coefficients. Consequently, there is an interval of critical wind skew angles for which the risk of vehicle accidents is maximised; in this study the critical range of β goes from 40° to 70° and it leads to yawing, side-slipping and overturning accident risk ratios that are, respectively, 25%, 28% and 45% higher than those observed under purely cross-winds. This is in agreement with the work of Baker [14] and with the mean values of $f^S_{v,w}$ presented in Section 2 for off-bridge scenarios. Therefore, it is important to consider a wide range of wind incidence angles in the W-VBI analysis, not only $\beta = 90°$ as it is routinely assumed. Indeed, none of the 10 independent analysis runs results in vehicle accidents for $\beta = 90°$ and above (tailwinds), but one of the records with $\beta = 55°$ led to a yawing accident ($\eta_Y > 1$). It is also noted that the dispersion of the accident risk ratios increases slightly for cross-winds due to the more significant vehicle-bridge interaction at the central span of the bridge.

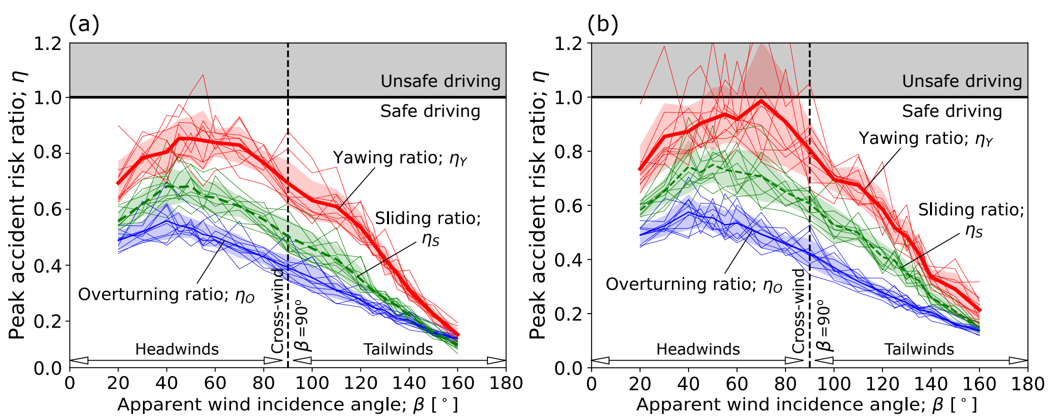

Figure 16: Peak accident risk ratios at any point of the deck in terms of the apparent wind incidence angle β for all the records: (a) original bridge, (b) modified case increasing the wind-induced forces on the deck 7 times. The thick lines represent the arithmetic mean and the colour bands ± one standard deviation around it; $\widehat{U}_b = 22.35$ m/s; $V_d = -64.4$ km/h.

The above observations on the influence of the wind incidence angle are inevitably linked to the aerodynamic response of the bridge under consideration. This structure represents a conventional prestressed concrete beam bridge with variable section for which wind-induced displacements are moderate. In order to investigate further the effect of these displacements on the driving safety without presenting an additional case study of a different structure, it is proposed to scale up the wind forces on the bridge deck by a factor of seven (i.e. $\mathbf{f}_{b,w} \times 7$), without altering the structure or the direct wind actions on the vehicle crossing it. Fig. 17 compares the time-history of the deck displacements at midspan under one of the wind velocity records before and after increasing the wind effects on the deck, without vehicle actions. The scaling factor of $\mathbf{f}_{b,w}$ in the new set of analysis is selected to increase the standard deviation of the vertical deck displacements at midspan to approximately 30 mm when $\beta = 90°$, which is approximately the value measured experimentally in the Third Nanjing Bridge (a 648-m span cable-stayed bridge in China) under cross-winds of the same intensity as in the proposed study [11]. This allows to observe the effect of the vehicle-bridge interaction on the driving accident risks without particularising on a specific structure, and facilitating the comparison with the previous results.

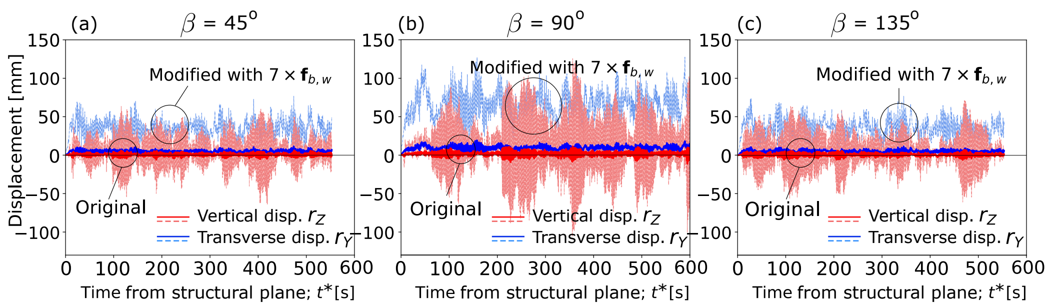

Figure 17: Time-history of the bridge displacements at midspan in the original structure and after increasing the wind-induced forces on its deck 7 times: (a) $\beta = 45°$, (b) $\beta = 90°$ and (c) $\beta = 135°$. $\widehat{U}_b = 22.35$ m/s; Sample Record #4; no vehicle included.

Figs. 16(a) and (b) compare the peak accident risk ratios in the original case study and in the modified W-VBI analysis with larger wind-induced deck displacements, respectively. The results indicate that the movements of the deck in long-span cable-supported bridges increase the risk of accidents for skew angles above 40°, particularly those related to sliding and yawing due to instantaneous wheel decompressions during the vehicle journey. The analysis with the increased deck displacements shows accidents in a number of records under headwinds, but the effect of the wind-induced vibrations in the deck is proportionally larger for tailwinds even though driving instabilities are not observed in those cases. This is because the direct wind actions on the vehicle are reduced when $\beta > 90°$, and therefore the vibration transferred directly from the deck to the vehicle becomes more prominent. Compared with the original case study in which the critical skew angle ranges from 40° to 70°, the highest accident risks in the case with larger deck displacements occur for $\beta = 70°$. This suggests that in very long-span bridges the critical wind incidence angles can be closer to $\beta = 90°$ than in stiffer structures because of the larger vibration introduced from the deck in the vehicle through the wheel/pavement contacts for purely cross-winds, but the direct effects of the wind on the vehicle for headwinds are still dominant. Therefore, it is concluded that purely cross-winds ($\beta = 90°$) are not critical for the driving safety regardless of the level of wind-induced movements in the deck.

7. Conclusions

This study proposes a new method to simulate three-dimensional fields of spatially-correlated wind velocity time-histories that are generally skew to the structure. It is based on the assumption of frozen turbulence and it reduces to the Veers' method [16] for the particular case of purely cross-winds. The generated wind fields are used to extend the conventional wind-vehicle-bridge interaction (W-VBI) analysis to skew wind scenarios, which are critical for the driving accident risks. The proposed methodology is applied to the study of vehicles crossing a long bridge to observe the following:

- The wind velocity time-history signals are generated in the projection of the structure to a plane that is perpendicular to the along-flow direction, which increases the spatial coherence of non-orthogonal winds. The signals are then referred to the plane of the structure by applying a time-lag that depends on the mean wind speed, and by rotating their horizontal wind components to the structural axes. The mean values of the resulting wind velocity fields are in agreement with the 'cosine' rule usually applied to skew winds, and the turbulence is consistent with the target frequency spectra and coherence functions.

- The specific nature of the W-VBI problem admits the use of the linear quasi-steady model to define the skew wind actions on the bridge deck. The buffeting components are calculated from accross-deck and vertical turbulence signals that are obtained by subtracting their mean values from the total wind speed generated in the proposed simulation of non-orthogonal winds.

- The results indicate that the lateral response of the deck is more influenced by the wind skew angle, and that it is maximised under purely cross-winds ($\beta = 90°$). The vertical response of the deck is also influenced by the angle of incidence of the wind because of buffeting and aeroelastic actions that are largest at the central span when $\beta = 90°$.

- Unlike in the bridge, the response of the vehicle is maximised under non-orthogonal wind actions. The critical aerodynamic coefficients of the vehicle for its driving instability are largest in tailwind conditions ($\beta > 90°$). Purely cross-winds ($\beta = 90°$) maximise the vehicle-bridge interaction, particularly if the displacements induced by wind in the deck are significant (as it can be the case in long-span bridges). However, the relative wind speed acting on the vehicle dominates its dynamic response and it is higher with headwinds ($\beta < 90°$). The risk of accidents of vehicles crossing straight bridges is maximised for wind skew angles in the interval from $\beta = 40°$ to $70°$.

Acknowledgements

This work derives from the project "Driving stability in the Orwell Bridge under high winds", funded by Highways England. Their support is greately appreciated. Note that the reported accident risks are not necessarily representative of the actual conditions in the Orwell Bridge.

Nomenclature

α_s Angle of attack between the wind and the structural section in static equilibrium

$\bar{\psi}$ Mean value of the relative wind incidence angle as the vehicle crosses the bridge

$\bar{f}^S_{v,w}$ Mean value of the side wind force on the vehicle as it crosses the bridge

$\bar{U}_r$ Mean value of the relative wind speed as the vehicle crosses the bridge

$\bar{U}_{y,j}, \bar{U}_{x,j}$ Across- and along-deck projections of the along-flow mean wind speed, respectively

β Apparent wind incidence angle (also referred to as yaw or skew angle)

$\boldsymbol{\phi}$ A mode shape of the structure

$\widehat{\boldsymbol{\phi}}^i$ Matrix with the phase angles of the wind signal in the direction i of the GP

$\boldsymbol{f}_{b,w-b}$ Buffeting wind force vector in the bridge

$\boldsymbol{f}_{b,w-se}$ Aeroelastic wind force vector in the bridge

$\boldsymbol{f}_{b,w-s}$ Mean wind force vector in the bridge

$\Delta\tilde{f}_{\mathrm{RMS}}$ Window width in the RMS average of the wind frequency spectra

Δf Width of the frequency bands in which $\widehat{\mathbf{S}}^i$ are discretised

Δn Frequency resolution in the generation of the pavement irregularities

Δt Time-step in the wind velocity records and in the W-VBI analysis

Δt_j Time-shift between the wind signals of the j-th node at the SP with respect its projection in the GP

Δx_{jr} Relative distance in the along-deck direction between the node j and a reference point r of the SP

δ Longitudinal projection of the distance between two points in the pavement irregularity surface

$\dot{p}, \dot{h}$ Lateral and vertical velocities of the 3-DOF deck sectional model

η_o, η_s, η_y Overturning, side-slipping and yawing accident risk ratios, respectively

γ^i_{jk} Coherence function between nodes j and k in the direction i of the SP under orthogonal winds

$\mathbf{\Phi}$ Matrix with the relevant mode shapes of the structure

$\widehat{\mathbf{A}}^i$ Matrix with the amplitudes of the wind signal in the direction i of the GP

$\widehat{\mathbf{S}}^i$ Projected spectral matrix associated with the i-th direction of the turbulence in the GP

$\widehat{\mathbf{V}}^i$ Complex coefficient matrix of the wind signals in the GP

$\mathbf{C}_l$ Damping matrix of the bridge ($l = b$) or the vehicle ($l = v$)

$\mathbf{f}_{l,r}$ Force vector due to the wheel-pavement contact in the bridge ($l = b$) or in the vehicle ($l = v$)

$\mathbf{f}_{l,w}$ Force vector due to the wind in the bridge ($l = b$) or in the vehicle ($l = v$)

$\mathbf{f}_{v,g}$ Force vector due to gravity in the vehicles

$\mathbf{K}_l$ Stiffness matrix of the bridge ($l = b$) or the vehicle ($l = v$)

$\mathbf{M}_l$ Mass matrix of the bridge ($l = b$) or the vehicle ($l = v$)

$\mathbf{q}_l$ Displacement vector of the bridge ($l = b$) or the vehicle ($l = v$)

μ_c Tyre-pavement friction coefficient

ψ Relative wind incidence angle on the vehicle

ρ Density of the air

σ_j^i Standard deviaton of the turbulent wind at node j in the i-th direction of the GP

$\sigma_1 - \sigma_6$ Parameters to calculate the aerodynamic coefficients of the vehicle

θ_m, ϕ_m Random phase angles used in the generation of the pavement irregularities

$\tilde{f}$ Reduced frequency used to define the wind spectra

$\widehat{\gamma}_{jk}^i$ Projected coherence function between nodes j and k in the direction i of the GP under skew winds

$\widehat{\phi}_{jm}^i$ Component of the matrix $\widehat{\boldsymbol{\phi}}^i$ corresponding to the node j and the frequency m

$\widehat{A}_{jm}^i$ Component of the matrix $\widehat{\mathbf{A}}^i$ corresponding to the node j and the frequency m

$\widehat{G}_{jj,\mathrm{RMS}}^i$ RMS wind frequency spectra at the node j in the GP direction i

$\widehat{G}^i_{jj}$ Symmetric PSD of the wind speed at node j in the GP direction i

$\widehat{S}^i_{jj}$ Auto-spectral component of the $\widehat{\mathbf{S}}^i$ matrix corresponding to the j-th node

$\widehat{S}^i_{jk}$ Cross-spectral component of the $\widehat{\mathbf{S}}^i$ matrix corresponding to the nodes j and k

$\widehat{U}$ Along-flow mean wind speed

$\widehat{u}, \widehat{v}, \widehat{w}$ Along-flow, across-flow and vertical wind turbulent components, respectively

$\widehat{U}_j$ Along-flow mean wind speed at the j-th node

$\widehat{u}_j, \widehat{v}_j, \widehat{w}_j$ Along-flow, across-flow and vertical wind turbulent components at the j-th node, respectively

$\widehat{U}_b$ Reference mean wind speed

$\widehat{U}_{jk}$ Arithmetic mean of the along-flow mean wind speeds at nodes j and k

$\widehat{U}_{z,10}$ Mean along-flow wind speed at $z = 10$ m

$\widehat{x}, \widehat{y}, \widehat{z}$ Across-flow, along-flow and vertical axes of the GP, respectively

$\widehat{x}_j, \widehat{y}_j, \widehat{z}_j$ Coordinates of the j-th node projected in the GP

ξ Modal damping ratio

A^i Parameters that define the Kaimal turbulence spectra

A_v Reference surface of the vehicle

B Width of the deck

b Half-distance between wheel lines in the transverse direction

C^b_D, C^b_L, C^b_M Drag, lift and moment static coefficients of the structure, respectively

$C^i_{\widehat{x}}, C^i_{\widehat{z}}$ Coherence decrements in the horizontal (across-flow) and the vertical directions of the GP, respectively

C_l^v Aerodynamic coefficients of the vehicle

$C_D^{b'}, C_L^{b'}, C_M^{b'}$ Derivatives of the drag, lift and moment static coefficients of the structure with respect to the angle of attack, respectively

D Depth of the deck

$d_{jk}, \widehat{d}_{jk}$ Distance between two generic nodes in the SP and its projection in the GP

f A vibration frequency of the structure

$f_{b,w-b}^D, f_{b,w-b}^L, f_{b,w-b}^M$ Buffeting drag, lift and moment induced by wind in the bridge, respectively

$f_{b,w-se}^D, f_{b,w-se}^L, f_{b,w-se}^M$ Self-excited drag, lift and moment induced by wind in the bridge, respectively

$f_{b,w-s}^D, f_{b,w-s}^L, f_{b,w-s}^M$ Mean drag, lift and moment induced by wind in the bridge, respectively

$f_{v,w}^l$ l-th component of the wind action on the vehicle

$F_{c,Z-F}^{\text{static}}, F_{c,Z-R}^{\text{static}}$ Static value of the vertical force in each of the wheels in the front and the rear vehicle axles, respectively

f_m central frequency of the m-th frequency band in which $\widehat{\mathbf{S}}^i$ are discretised

$F_{c,Y-F}, F_{c,Z-F}$ Sum of the lateral and the vertical forces in the front wheels, respectively

$F_{c,Y-R}, F_{c,Z-R}$ Sum of the lateral and the vertical forces in the rear wheels, respectively

$F_{c,Y-wh}$ Lateral force at the contact between the pavement and the wheel wh

$F_{c,Z-L}$ Sum of the vertical force in all the leeward wheels

$F_{c,Z-wh}$ Vertical force at the contact between the pavement and the wheel wh

$F_{c,Z-W}$ Sum of the vertical force in all the windward wheels

G_d Target one-sided PSD of displacements in the pavement irregularities

$G_{d,x}$ One-sided cross PSD function of displacements in the pavement irregularities

h_v Distance between the vehicle centroid and the tyre/pavement contact

I_j^i Turbulence intensities at node j in the i-th direction of the GP

L^i Turbulence length scale in the i-th direction of the GP

n_0 Reference spatial frequency in the generation of the pavement irregularities

n_1, n_{N_m} Lower and upper frequency bounds in the generation of the pavement irregularities, respectively

N_f Number of frequency bands in which $\widehat{\mathbf{S}}^i$ are discretised

n_m Discrete spatial frequency of the pavement irregularity

N_n Number of discrete spatial frequencies included in the pavement irregularities

N_p Number of points in which wind is simulated

N_r Number of independent wind and pavement irregularity records generated

p, h, α Lateral, vertical and torsional movements of the 3-DOF deck sectional model, respectively

R Autocorrelation function of the pavement irregularity profile

r_L, r_W Pavement irregularity profiles in the leeward and the windward wheels, respectively

t, t^* Reference time at the GP and at the SP, respectively

$u^{tot}, v^{tot}, w^{tot}$ Across-deck, along-deck and vertical components of the total wind speed, respectively

$u_j^{tot}, v_j^{tot}, w_j^{tot}$ Across-deck, along-deck and vertical components of the total wind speed at the j-th node, respectively

u_j, v_j, w_j Across-deck, along-deck and vertical wind turbulence components, respectively

U_r Relative wind velocity acting on the vehicle

V_d Vehicle driving speed

x, y, z Along-deck, across-deck and vertical axes of the SP, respectively

x_j, y_j, z_j Coordinates of the j-th node in the SP

References

[1] R. Pritchard, Wind effects on high sided vehicles, Journal of Institute of Highway Transportation 56 (1985) 22–25.

[2] Y. Xu, W. Guo, Dynamic analysis of coupled road vehicle and cable-stayed bridge systems under turbulent wind, Engineering Structures 25 (2003) 473–486.

[3] C. Cai, S. Chen, Framework of vehicle-bridge-wind dynamic analysis, Journal of Wind Engineering and Industrial Aerodynamics 92 (7/8) (2004) 579–607.

[4] S. Chen, C. Cai, Accident assessment of vehicles on long-span bridges in windy environments, Journal of Wind Engineering and Industrial Aerodynamics 92 (2004) 991–1024.

[5] A. Camara, I. Kavrakov, K. Nguyen, G. Morgenthal, Complete framework of wind-vehicle-bridge interaction with random road surfaces, Journal of Sound and Vibration 458 (2019) 197–217.

[6] R. Scanlan, Estimates of skew wind speeds for bridge flutter, Journal of Bridge Engineering 4 (2) (1999) 95–98.

[7] L. Zhu, Y. Xu, F. Zhang, H. Xiang, Tsing Ma bridge deck under skew winds - part I: aerodynamic coefficients, Journal of Wind Engineering and Industrial Aerodynamics 90 (2002) 781–805.

[8] L. Zhu, Y. Xu, H. Xiang, Tsing Ma bridge deck under skew winds - part II: flutter derivatives, Journal of Wind Engineering and Industrial Aerodynamics 90 (2002) 807–837.

[9] A. Davenport, N. Isyumov, D. Fader, C. Bowen, A study of wind action on a suspension bridge during erection and on completion: The Narrows bridge, Tech. rep., BLWT-3-69, University of Western Ontario, Canada, eng. Sci. Res. Rep. (1969).

[10] H. Tanaka, A. Davenport, Response of taut strip models to turbulent wind, Journal of Engineering Mechanics ASCE 108 (1) (1982) 33–49.

[11] L. Zhu, M. Wang, D. Wang, Z. Guo, F. Cao, Flutter and buffeting performances of Third Nanjing bridge over Yangtze river under yaw wind via aeroelastic model test, Journal of Wind Engineering and Industrial Aerodynamics 95 (2007) 1579–1606.

[12] J. Xie, H. Tanaka, R. Wardlaw, M. Savage, Buffeting analysis of long span bridges to turbulent wind with yaw angle, Journal of Wind Engineering and Industrial Aerodynamics 37 (1991) 65–77.

[13] M. Batista, M. Perkovic, A simple static analysis of moving road vehicle under cross wind, Journal of Wind Engineering and Industrial Aerodynamics 128 (2014) 105–113.

[14] C. Baker, Measures to control vehicle movement at exposed sites during windy periods, Journal of Wind Engineering and Industrial Aerodynamics 25 (1987) 151–161.

[15] S. Kim, C. Yoo, H. Kim, Vulnerability assessment for the hazards of cross-winds when vehicles cross a bridge, Journal of Wind Engineering and Industrial Aerodynamics 156 (2016) 62–71.

[16] P. Veers, Three-dimensional wind simulation, Tech. rep., Sandia National Laboratories, California, U.S., sAND88-0152, UC-261 (1988).

[17] M. Shinozuka, C. Jan, Digital simulation of random processes and its applications, Journal of Sound and Vibration 25 (1) (1972) 111–128.

[18] A. Camara, A fast mode superposition algorithm and its application to the analysis of bridges under moving loads, Advances in Engineering Software 151 (2021) 102934.

[19] C. Dodds, J. Robson, The description of road surface roughness, Journal of Sound and Vibration 31 (2) (1973) 175–183.

[20] M. Sayers, Dynamic terrain inputs to predict structural integrity of ground vehicles, Tech. rep., University of Michigan / Transportation Research Institute (Rep. No. UMTRI-88-16), Ann Arbor,MI, organizational Results Research Report (0R08.003) (1988).

[21] A. Davenport, The response of slender, line-like structures to a gusty wind, Proceedings of the Institution of Civil Engineers 23 (3) (1962) 389–408.

[22] R. Scanlan, Motion-related body-force functions in two-dimensional low-speed flow, Journal of Fluids and Structures 14 (2000) 49–63.

[23] I. Kavrakov, A. Camara, G. Morgenthal, Influence of aerodynamic model assumptions on the wind-vehicle-bridge interaction, in: IABSE Symposium, Stockholm, 2016.

[24] H. Tang, Y. Li, K. Shum, Flutter performance of long-span suspension bridges under non-uniform inflow, Advances in Structural Engineering 21 (2) (2018) 201–213.

[25] ABAQUS, User's manual, version 2020x (2020).

[26] EC1, Eurocode 1: Actions on structures - part 1-4: General actions - wind actions, EN 1991-1-4:2005 (2005).

[27] UK National Annex to Eurocode 1: Actions on structures, Part 1-4: General Actions - Wind Actions (2010).

[28] BS6399: Part 2: Loading for buildings: Part 2: Code of practice for wind loads (1996).

[29] E. Strömmen, Theory of bridge aerodynamics. Second Edition, Springer, 2010.

[30] A. Camara, V. Vazquez, A. Ruiz-Teran, S. Paje, Influence of the pavement surface on the vibrations induced by heavy traffic in road bridges, Canadian Journal of Civil Engineering 12 (44) (2017) 1099–1111.

[31] G. Solari, G. Piccardo, Probabilistic 3-D turbulence modeling for gust buffeting of structures, Probabilistic Engineering Mechanics 16 (2001) 73–86.

[32] FLUENT, ANSYS user's manual, version 2019 R1 (2019).

[33] ISO 8608:1995: Mechanical vibration - Road surface profiles - Reporting of measured data (1995).

[34] E. Jones, R. Childers, Contemporary College Physics, 3rd Edition, McGraw-Hill Education (ISE Editions), 2001.